

# Secondary Eyewall Formation in an Idealized Tropical Cyclone Simulation: Balanced and Unbalanced Dynamics

HUI WANG AND CHUN-CHIEH WU

*Department of the Atmospheric Sciences, National Taiwan University, Taipei, Taiwan*

YUQING WANG

*International Pacific Research Center, and Department of Atmospheric Sciences, University of Hawai'i at Mānoa, Honolulu, Hawaii*

(Manuscript received 29 May 2015, in final form 20 June 2016)

## ABSTRACT

The secondary eyewall formation (SEF) in an idealized simulation of a tropical cyclone (TC) is examined from the perspective of both the balanced and unbalanced dynamics and through the tangential wind ( $V_t$ ) budget analysis. It is found that the expansion of the azimuthal-mean  $V_t$  above the boundary layer occurs prior to the development of radial moisture convergence in the boundary layer. The  $V_t$  expansion results primarily from the inward angular momentum transport by the mid- to lower-tropospheric inflow induced by both convective and stratiform heating in the spiral rainbands. In response to the  $V_t$  broadening is the development of radial inflow convergence and the supergradient flow near the top of the inflow boundary layer. Results from the  $V_t$  budget analysis show that the combined effect of the mean advection and the surface friction is to spin down  $V_t$  in the boundary layer, while the eddy processes (eddy radial and vertical advection) contribute positively to the spinup of  $V_t$  in the SEF region in the boundary layer. Therefore, eddies play an important role in the spinup of  $V_t$  in the boundary layer during SEF. The balanced Sawyer–Eliassen solution can well capture the secondary circulation in the full-physics model simulation. The radial inflow diagnosed from the Sawyer–Eliassen equation is shown to spin up  $V_t$  and maintain the vortex above the boundary layer. However, the axisymmetric balanced dynamics cannot explain the spinup of  $V_t$  in the boundary layer, which results mainly from the eddy processes.

## 1. Introduction

The secondary (concentric) eyewall, identified as the presence of a secondary convective ring with its associated secondary tangential wind maximum, is one of the important features in intense tropical cyclones (TCs). This phenomenon has been well documented based on passive satellite microwave and radar imagery (e.g., Hawkins and Helveston 2008; Kossin and Sitkowski 2009; Kuo et al. 2009; Hense and Houze 2012). Hawkins and Helveston (2008) analyzed a 10-yr multisensor dataset (1997–2006) and showed that 80% of the western Pacific, 70% of the Atlantic, 50% of the eastern Pacific, and 40% of the Southern Hemisphere intense

storms ( $>120$  knots;  $1 \text{ kt} = 0.51 \text{ m s}^{-1}$ ) experienced at least one concentric eyewall during their lifetime. Based on flight observations in the North Atlantic, the behavior of concentric eyewalls and their associated intensity change have been extensively investigated (Willoughby et al. 1982; Houze et al. 2006, 2007; Hense and Houze 2012; Bell et al. 2012). The storm usually weakens during the formation and intensification phases of a concentric eyewall, and four possible mechanisms associated with the demise of the inner eyewall are discussed by Rozoff et al. (2008). Once the outer eyewall replaces the inner one, the storm often reintensifies.

Based on high-resolution numerical models, a number of studies have focused on the secondary eyewall formation (SEF) and the subsequent eyewall replacement cycle (ERC). A couple of mechanisms were proposed in earlier studies, such as the topographic forcing (Hawkins 1983), the inertial instability in the outflow layer (Willoughby 1979), and the finite-amplitude wind-induced

---

*Corresponding author address:* Dr. Chun-Chieh Wu, Department of Atmospheric Sciences, National Taiwan University, No. 1, Sec. 4, Roosevelt Rd., Taipei 106, Taiwan.  
E-mail: cwu@typhoon.as.ntu.edu.tw

surface heat exchange (WISHE) instability triggered by external forcing in the upper troposphere (Nong and Emanuel 2003). Terwey and Montgomery (2008) pointed out that the above processes cannot be considered as essential for SEF, although they could affect the storm structure and intensity. Instead, they proposed that the process of beta-skirt axisymmetrization (BSA), in which the secondary wind maximum is generated through the anisotropic upscale cascade of convectively generated vorticity anomalies in the beta-skirt region.

There is no consensus so far as to what the leading dynamical mechanism responsible for SEF is. Recently, studies have been focused more on the internal dynamics that potentially govern SEF, such as the stagnation radius of the vortex Rossby wave (VRW) energy dispersion (Montgomery and Kallenbach 1997; Martinez et al. 2010, 2011; Menelaou et al. 2013; Qiu et al. 2010; Wang et al. 2013; Sun et al. 2013), the dynamical response of a balanced vortex to latent heating outside the eyewall (Wang 2009; Moon and Nolan 2010; Fang and Zhang 2012; Rozoff et al. 2012; Sun et al. 2013; Abarca and Montgomery 2014; Zhu and Zhu 2014), and the unbalanced dynamics within the boundary layer (Huang et al. 2012; Abarca and Montgomery 2013, 2014; Kepert 2013; Kepert and Nolan 2014; Montgomery et al. 2014; Qiu and Tan 2013; Sun et al. 2013; Wang et al. 2013).

Similar to quite a number of previous studies, this work defines the balanced dynamics as the component that can be recovered by the solution of the azimuthal-mean Sawyer–Eliassen equation. The residual from the balanced component is defined as the unbalanced dynamics. Note that this definition is slightly different from some other studies since we define the basic vortex as the azimuthal mean of the full-physics Weather Research and Forecasting (WRF) Model simulation, and the vortex might not be exactly in hydrostatic and gradient balance, in particular in the frictional boundary layer. This deviates from the definition recently discussed in Bui et al. (2009) and Abarca and Montgomery (2014). Abarca and Montgomery (2014) referred to the unbalanced flow as the axisymmetric part of the flow that does not satisfy the thermal wind balance. Nevertheless, our definition is consistent with many other studies (Montgomery et al. 2006; Fudeyasu and Wang 2011; Sun et al. 2013; Zhu and Zhu 2014).

Shapiro and Willoughby (1982) showed that a secondary circulation and spinup of the tangential wind could be induced by a point source of heat in a balanced TC-like vortex. Wang (2009) indicated that enhanced latent heating in outer rainbands would favor SEF in intense TCs. Similar results were also found in several other studies (Hill and Lackmann 2009; Judt and Chen

2010). Moon and Nolan (2010) hypothesized that if the imposed heating lasts long enough in rainbands outside the primary eyewall, the induced locally accelerated tangential wind can wrap around the entire vortex and cause SEF. Fang and Zhang (2012) found that the beta shear could lead to the formation of an extensive stratiform region outside of the primary eyewall; convection on the inner edge of the stratiform region becomes axisymmetrized and causes the TC to evolve into a secondary eyewall-like structure because of the weakening of the beta shear.

From the perspective of balanced dynamics, the transverse secondary circulation and the associated low-level convergence are induced by the radial gradient of diabatic heating. Rozoff et al. (2012) followed the work of Shapiro and Willoughby (1982) and showed that the sustained azimuthal-mean latent heating along with enhanced inertial stability outside the primary eyewall can lead to SEF. Zhu and Zhu (2014) proposed that heating in rainbands plays an important role in governing the formation and the development of the secondary tangential wind maximum. They also suggested that the secondary eyewall could not form unless the rainband convection reaches a certain strength relative to the eyewall convection.

Huang et al. (2012) proposed a new pathway of SEF based on a model–observation-consistent and high-spatial- and temporal-resolution dataset derived from Wu et al. (2012), who used the ensemble Kalman filter (EnKF) to assimilate The Observing System Research and Predictability Experiment (THORPEX) Pacific Asian Regional Campaign (T-PARC) data. The unbalanced response within and just above the boundary layer to the expanding swirling wind was shown as an important mechanism for concentrating and sustaining deep convection in a narrow supergradient wind zone in the outer-core region of the TC, and thus for SEF. Furthermore, Abarca and Montgomery (2013) demonstrated that the boundary layer unbalanced dynamics alone can generate a secondary wind maximum outside the primary eyewall in an axisymmetric nonlinear slab boundary layer model, providing further supporting evidence for the dynamical pathway shown in Huang et al. (2012). Furthermore, Wang et al. (2013) conducted an idealized simulation and also found a strong positive net radial force (namely, the unbalanced component in the radial momentum equation) in the boundary layer during SEF, supporting the idea that the unbalanced boundary layer dynamics play a crucial role in SEF.

Recently, Kepert (2013) and Kepert and Nolan (2014) found that weak local enhancement of the radial vorticity gradient outside of the primary radius of maximum wind (RMW) can generate a significant frictional updraft, even

if there is no broadening of the tangential wind above the boundary layer. They proposed a positive feedback between the local enhancement of the radial vorticity gradient, the frictional updraft, and convection. [Kepert \(2013\)](#) also hypothesized that the boundary layer contributes to rather than initiates the secondary eyewall formation. Recent studies have examined both the balanced response to diabatic heating and the unbalanced dynamics within the boundary layer during SEF in TCs. Using the Doppler radar data collected from the secondary eyewall of Hurricane Rita (2005), [Didlake and Houze \(2011\)](#) found that both the mean and perturbation motions strengthen the secondary wind maximum, but they have different roles. Based on multiplatform observations, [Bell et al. \(2012\)](#) found that the spinup of tangential wind in Hurricane Rita (2005) occurred not only within but also above the boundary layer. They suggested that both the balanced and unbalanced dynamics play important roles in the SEF of Hurricane Rita (2005) but did not evaluate their respective contributions. [Sun et al. \(2013\)](#) found that the development and the subsequent inward movement of outer rainbands and the unbalanced boundary layer dynamics all contributed to the SEF in a simulation of Typhoon Sinlaku (2008). [Qiu and Tan \(2013\)](#) showed that the inward movement of outer rainbands could induce strong asymmetric inflow in the boundary layer, thus enhancing supergradient winds and convergence through the asymmetric process, while axisymmetrization of the bands leads to SEF in the end.

The relative importance of the balanced and unbalanced dynamics to SEF is still unknown. Different from the findings of [Rozoff et al. \(2012\)](#) and [Zhu and Zhu \(2014\)](#), with the aid of the Sawyer–Eliassen equation, [Abarca and Montgomery \(2014\)](#) examined the departure from the axisymmetric balanced dynamics during SEF and found that the balanced dynamics could not capture the tangential wind spinup in the lower troposphere as exhibited in the full-physics model simulation. The issue regarding the importance of balanced dynamics versus unbalanced dynamics in SEF remains to be examined, since different TC cases were analyzed and different model settings were used in the numerical simulations above.

The present study aims to clarify the relative importance of the balanced and unbalanced dynamics in spinning up the secondary tangential wind maximum in the SEF region based on an idealized high-resolution, full-physics simulation of a TC using the WRF Model. The simulated SEF is diagnosed in detail based on the azimuthal-mean tangential wind budget and the Sawyer–Eliassen equation. [Section 2](#) briefly describes the configuration of the WRF Model. The SEF and the asymmetric evolution of the simulated TC are discussed

in [section 3](#). [Section 4](#) presents analyses of the unbalanced dynamics within and above the boundary layer. In [section 5](#), the forcing sources for the balanced Sawyer–Eliassen equation and its solution are analyzed by focusing on the balanced tangential wind budget. Conclusions are drawn in the last section.

## 2. Numerical model and experimental design

The idealized numerical experiment is conducted using the WRF Model, version 3.5.1, which is a mesoscale model designed for both full-physics real-case and idealized simulations. The model domain is quadruply nested with grid spacings of 45-, 15-, 5-, and 1.67-km for the four meshes, with  $200 \times 200$ ,  $250 \times 250$ ,  $268 \times 268$ , and  $388 \times 388$  grid points, respectively. There are 36 vertical levels extending from the ocean surface with an unperturbed surface pressure of 1010 hPa up to the model top of 50 hPa in the mass vertical coordinates. To reduce the artificial wave reflection near the lateral boundaries, the outermost domain ( $9000 \text{ km} \times 9000 \text{ km}$ ) is set to be large enough to prevent gravity wave reflection from the lateral boundaries. The innermost domain is about  $647 \text{ km} \times 647 \text{ km}$ , large enough to cover both the vortex inner core and outer rainbands. The three inner nested meshes are located at the center of their parent domains, and the vortex-following technique is activated to allow for long-term integrations.

The model is initiated with an axisymmetric cyclonic vortex formulated by [Wang and Li \(1992\)](#) and placed on an  $f$  plane of  $20^\circ\text{N}$ . There is no background atmospheric flow, and the ocean is homogeneous, with a fixed sea surface temperature (SST) of  $29^\circ\text{C}$ . The initial temperature and moisture profiles of the unperturbed environmental atmosphere are constructed based on the western Pacific clear-sky environment given by [Gray et al. \(1975\)](#). The maximum tangential wind is set to be  $20 \text{ m s}^{-1}$  at a radius of 120 km, and the tangential wind is diminished to zero at the radius of 600 km. The mass and the thermodynamic fields are obtained by adjusting the vortex to gradient wind and hydrostatic balances.

In this simulation, the WRF single-moment 6-class microphysics scheme (WSM6; [Hong and Lim 2006](#)) is applied to all meshes. The Yonsei University (YSU) planetary boundary layer scheme ([Hong et al. 2006](#)) is used to parameterize turbulent vertical mixing. The Kain–Fritsch cumulus parameterization scheme ([Kain and Fritsch 1993](#)) is used on the two outer meshes, but not on the inner two meshes, in which strong and deep convection is considered to be resolved explicitly. The radiation is calculated using the Dudhia scheme for shortwave ([Dudhia 1989](#)) and the Rapid Radiative Transfer Model (RRTM) for longwave ([Mlawer et al. 1997](#)).

The model is integrated forward for 192 h, with the model output at 1-h intervals. The first 48 h is considered as the spinup period, in which the structure of the vortex evolves to one that is similar to a real TC. Detailed results of structure evolution of the TC after the spinup period are presented in the following sections.

### 3. An overview of the simulated SEF

Figure 1 shows the sequence of the simulated reflectivity at 3-km height before and during the onset of the SEF at 3-h intervals. At 109 h (Fig. 1d), the vortex exhibits a clear eye with a radius of 30 km, which is surrounded by an eyewall with enhanced convective activity. Isolated convective cells (regarded as part of the outer spiral rainbands), which are sporadically distributed outside the 120-km radius, develop actively in accordance with the generation of the convective available potential energy (CAPE; Fig. 2b) and rotate cyclonically around the vortex center in the form of outer spiral rainbands. This is consistent with the findings of Li and Wang (2012), who showed that the detached inner rainbands can act as a trigger for vigorous deep convection and can be reorganized into outer spiral rainbands if the ambient CAPE is large. The enhanced CAPE begins at 96 h and only lasts until 120 h. In response to this enhanced CAPE, the rainbands expand not only in the radial direction (width), but also in the azimuthal direction (length) in the simulation. At 112 h, a primary spiral rainband is located at around 167-km radius with a width of 120 km and covers three (northeast, northwest, and southwest) quadrants (Fig. 1e). The outer rainbands become elongated in the azimuthal direction gradually, and eventually an individual annular eyewall structure forms at a radius of approximately 80 km at 120 h, which is defined as the time of the SEF in the following sections. Afterward, the ERC occurs as the secondary eyewall continues to intensify and contract while the primary eyewall weakens and eventually vanishes at 162 h, after which the secondary eyewall becomes the primary eyewall (Fig. 2a). The evolution of spiral rainbands prior to SEF strongly suggests that both diabatic heating and asymmetric eddies in spiral rainbands play critical roles in SEF. This will be further diagnosed in sections 4 and 5 below.

Figure 2 shows the time–radius Hovmöller diagrams (from 48 to 192 h) of the azimuthal-mean storm structure. Outside the primary eyewall, diffuse radar reflectivity (at 3 km) (Fig. 2a) begins to develop from a radius of about 50 km after 48 h of simulation and continues to propagate radially outward, indicating the gradual development of the inner rainbands. With progressive enhancement of the radial inflow (Fig. 4) collocated with the region where the tangential wind field is

broadened radially outward (Fig. 2c), the first less-significant SEF with a weak moat occurs at around 84 h. The first SEF and the subsequent ERC are completed in about 12 h, but the associated secondary wind maximum is hard to identify since the first secondary eyewall forms so close to the primary eyewall (Fig. 2c). A possible explanation is that the expansion/intensification/strengthening of the tangential wind is not significant enough as compared to the second SEF (the one beginning at 120 h). To be clear, two SEF events occurred during this long-term simulation, but the focus of this study is on the second SEF, which is more pronounced.

Along with the inward movement of the first secondary eyewall, which merges with the primary eyewall at around 100 h, moderate convection associated with inner rainbands develops progressively and propagates outward from around 90 to 140 km in radius (Fig. 2a) after 96 h. The outer rainbands, which are located farther outward (150–200 km), begin to develop at 110 h and then contracts inward over the next 10 h. The SEF occurs when a distinct secondary peak in tangential wind and vertical velocity (larger than  $0.5 \text{ m s}^{-1}$ ) appears at 120 h. The secondary eyewall contracts inward with time after its formation. The inner eyewall eventually disappears at about 162 h and is replaced by the outer eyewall. The second ERC lasts for almost 42 h in the simulation, which is longer than the typical time from both observation and other modeling studies.

Figure 2b shows the time evolution of the azimuthal-mean vertical motion at 3-km height and CAPE. Coincident with the azimuthal-mean radar reflectivity (Fig. 2a), a distinct secondary peak in vertical velocity (larger than  $0.5 \text{ m s}^{-1}$ ) appears at the radial band between 90 and 125 km from the vortex center at 120 h, indicating the formation of the secondary eyewall. In agreement with the findings in Rogers et al. (2012) and Qiu and Tan (2013), the development and enhancement of convection in outer rainbands is manifested by vertical motion larger than  $0.5 \text{ m s}^{-1}$ . Prior to the SEF (96–120 h), the region outside the primary eyewall is thermodynamically favorable for the sustained convective activity, with CAPE being generally larger than  $1200 \text{ J kg}^{-1}$ . When the secondary peak in vertical motion occurs, CAPE outside the primary eyewall begins to decrease, as it is largely consumed by convection in the new secondary eyewall. After the SEF, the upward motion of the secondary eyewall is enhanced, while that in the primary eyewall weakens and eventually is replaced by the secondary eyewall after about 42 h of the coexistence of the two eyewalls.

Figure 2c shows the azimuthal-mean tangential wind at 1.5-km height. Initially, after the 48-h spinup, the

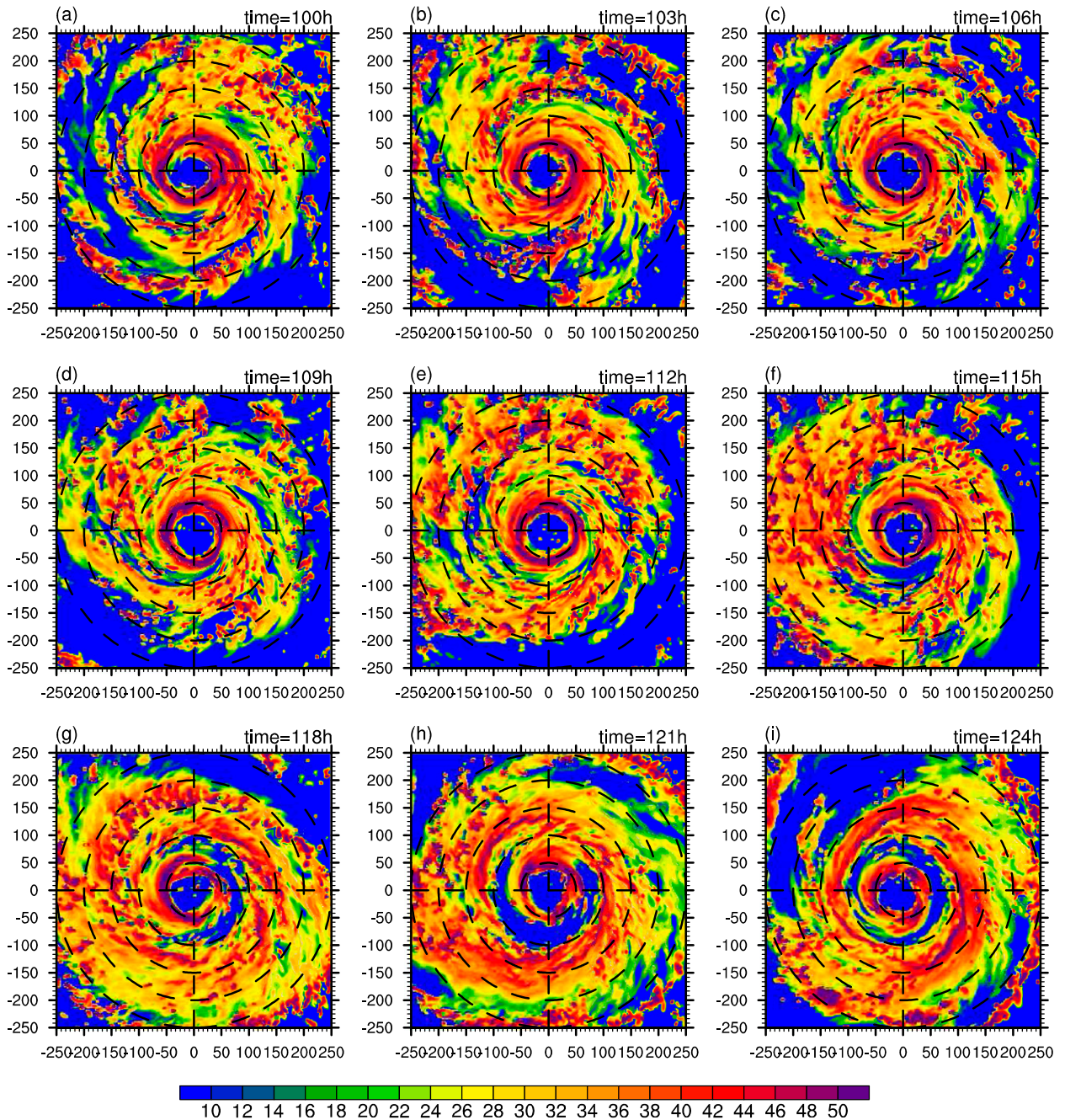


FIG. 1. Plan view of the model-derived radar reflectivity (shaded; dBZ) at 3-km height from 100 to 124 h with a 3-h interval. The five concentric circles in each panel indicate the radii of 50, 100, 150, 200, and 250 km from the storm center. Model time is noted at the top right of each panel.

RMW is located at approximately 40-km radius with a maximum wind speed over  $40 \text{ m s}^{-1}$ . The  $40 \text{ m s}^{-1}$  contour extends from the 100-km radius at 72 h to the nearly 250-km radius at 120 h, exhibiting a steady increase in vortex size. A similar increase in the size of the inner core was found in the simulated Typhoon Megi (2010) by Wang and Wang (2013). At 120 h, a local secondary

peak in the azimuthal-mean tangential wind emerges, indicating the SEF. The tangential wind of the primary eyewall weakens as the secondary tangential wind maximum emerges and contracts inward (Fig. 2c). While an expanded range of the tangential wind is suggested to be a precursor of SEF from previous studies (Huang et al. 2012; Rozoff et al. 2012; Abarca and Montgomery

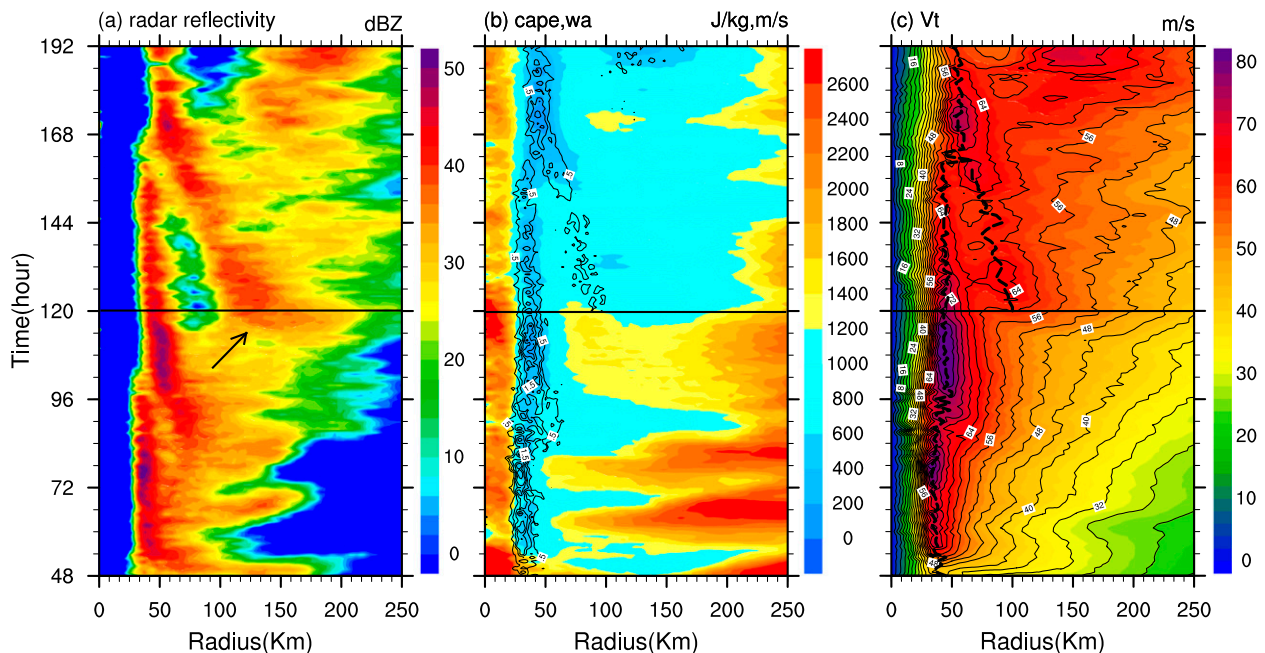


FIG. 2. Time–radius Hovmöller diagrams of the azimuthal-mean (a) radar reflectivity (shaded; dBZ) at 3 km, (b) CAPE (shaded;  $\text{J kg}^{-1}$ ) and vertical velocity (contour;  $\text{m s}^{-1}$ ) at 1 km with a  $0.5 \text{ m s}^{-1}$  interval, and (c) tangential wind ( $\text{m s}^{-1}$ ) at 1.5 km with a  $4 \text{ m s}^{-1}$  interval. The black line highlights the SEF time, and the black arrow indicates the outward movement of the inner rainbands.

2013), it is still not clear whether this factor is indeed the precursor of SEF or rather the consequence of it. In this study, we follow the convention in defining the time of first appearance of the secondary maximum in the azimuthal-mean tangential wind as the time of the SEF. The secondary maximum in the azimuthal-mean upward motion (larger than  $0.5 \text{ m s}^{-1}$ ) shows up at the same time.

Figure 3 illustrates radial–height cross sections of the azimuthal-mean tangential wind and vertical velocity between 110 and 126 h of simulation at 2-h intervals. At 110 h, when the storm is characterized by a mature TC with a single eyewall, the maximum tangential wind surpasses  $80 \text{ m s}^{-1}$  near the top of the inflow boundary layer at a radius of approximately 40 km. The strongest vertical velocity in the primary eyewall tilts radially outward from the 40-km radius at the 0.2-km height to the 65-km radius at the 15-km height, located slightly inside of the tangential wind maximum at each level. The tangential wind expands in both radius and height during the evolution of the vortex, as we can see from the  $40 \text{ m s}^{-1}$  tangential wind contour (Figs. 3a–f). Meanwhile, convective cells outside the primary eyewall become more active and more organized in the region of the SEF, as we can see from the area with vertical velocity above  $0.5 \text{ m s}^{-1}$  in the lower troposphere during 112–116 h. At 120 h, the vertical motion shows a ring-shaped structure and extends vertically throughout the troposphere, indicating the beginning of the SEF.

Concurrently, the range of the tangential wind continues to grow, and a secondary tangential wind maximum becomes more discernible between 83- and 125-km radii by 120 h. After 120 h, the secondary maximum in vertical velocity strengthens, and the corresponding ring-shaped upward motion also intensifies significantly, while vertical velocity in the primary eyewall weakens gradually.

#### 4. Dynamical processes within and above the boundary layer

Figure 4 shows the radius–height cross sections of the azimuthal-mean radial wind, vertical velocity, and horizontal divergence at 2-h intervals from 110 to 120 h. This period is regarded as a critical period prior to the SEF. The primary eyewall features the strongest inflow ( $-28 \text{ m s}^{-1}$ ) confined below the 1.5-km height and the enhanced upward motion from the lower to upper troposphere, collocated with the strongest convergence in the lower troposphere (Fig. 4a). As mentioned in section 3, tangential winds expand outward prior to the SEF. Here we can see that the boundary layer inflow in the outer region strengthens correspondingly (Figs. 4a–d). A secondary peak in the boundary layer inflow ( $-20 \text{ m s}^{-1}$ ) first appears between 120- and 140-km radii at 116 h (Fig. 4d). Furthermore, convergence (divergence) in (above) the boundary layer outside the primary eyewall strengthens with time (Figs. 4a–f).

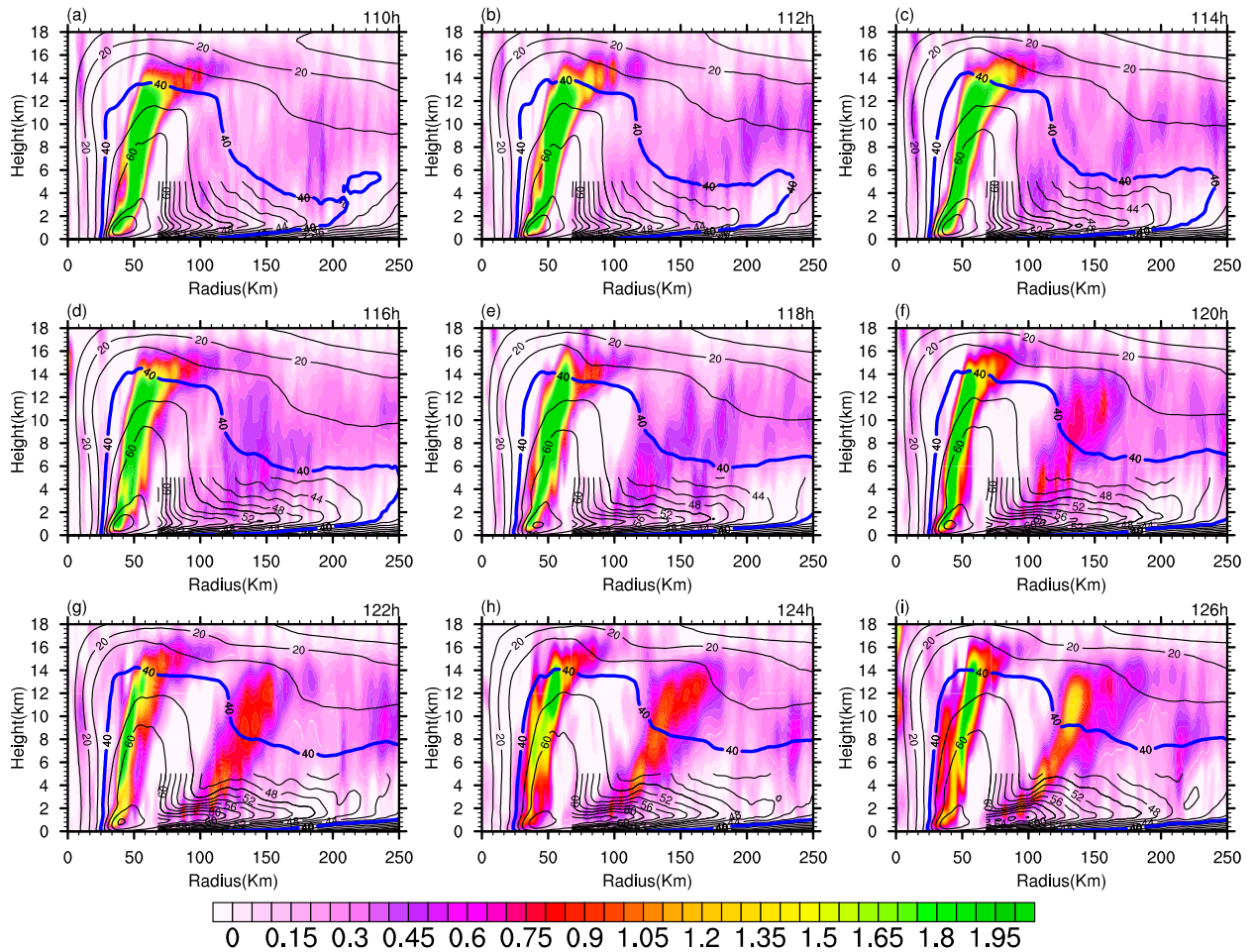


FIG. 3. Radius–height cross sections of the azimuthal-mean vertical motion (shaded;  $\text{m s}^{-1}$ ) and tangential wind (contours;  $\text{m s}^{-1}$ ) from 110 to 126 h at 2-h intervals. Contours are plotted every  $10 \text{ m s}^{-1}$ , except for the radius larger than 67 km and height lower than 5 km where the interval is  $2 \text{ m s}^{-1}$ . The blue contour indicates the  $40 \text{ m s}^{-1}$  tangential wind.

Vertical velocity exceeding  $0.5 \text{ m s}^{-1}$  appears farther outward in the SEF region and becomes organized in a radial band by 116 h (Fig. 4d). At 118 h (Fig. 4e), the secondary maximum in the boundary layer inflow ( $-20 \text{ m s}^{-1}$ ) shifts radially inward to the SEF region, collocated with the strengthened upward motion and enhanced low-level convergence. Strong convergence in the SEF region is associated with the rapid strengthening of the boundary layer inflow farther outward and the sudden deceleration near the inner edge of the SEF region. The enhanced upward motion is largely tied to the strong convergence rooted in the boundary layer. As the boundary layer convergence strengthens, the upward motion develops quickly with significantly reduced outward tilt, showing an eyewall-like structure by 120 h (Fig. 4f). This demonstrates that the boundary layer dynamics play a critical role in strengthening deep convection in previously existing outer rainbands and thus the SEF.

It is interesting to compare the overall evolution of the radial inflow in the SEF region (between 83- and 116-km radii) and that in the region immediately outside of the region (between 116- and 150-km radii). Figure 5 shows the azimuthal-mean radial wind averaged in the above two regions from 100 to 121 h at 3-h intervals (Figs. 5a,b). The strength of the boundary layer inflow in the SEF region does not change much during the 21-h period (only slightly intensifies when the secondary peak in the boundary layer inflow begins to shift radially inward after the SEF). In sharp contrast, the boundary layer inflow strengthens significantly and increases by  $5 \text{ m s}^{-1}$  immediately outside the SEF region (between 116- and 150-km radii) from 110 to 120 h (Fig. 5b). Meanwhile, the outflow immediately above the boundary layer strengthens significantly and is increased by about  $7 \text{ m s}^{-1}$  in the SEF region. The development of the strong shallow outflow above the top of the boundary layer is primarily due to the supergradient wind (to be

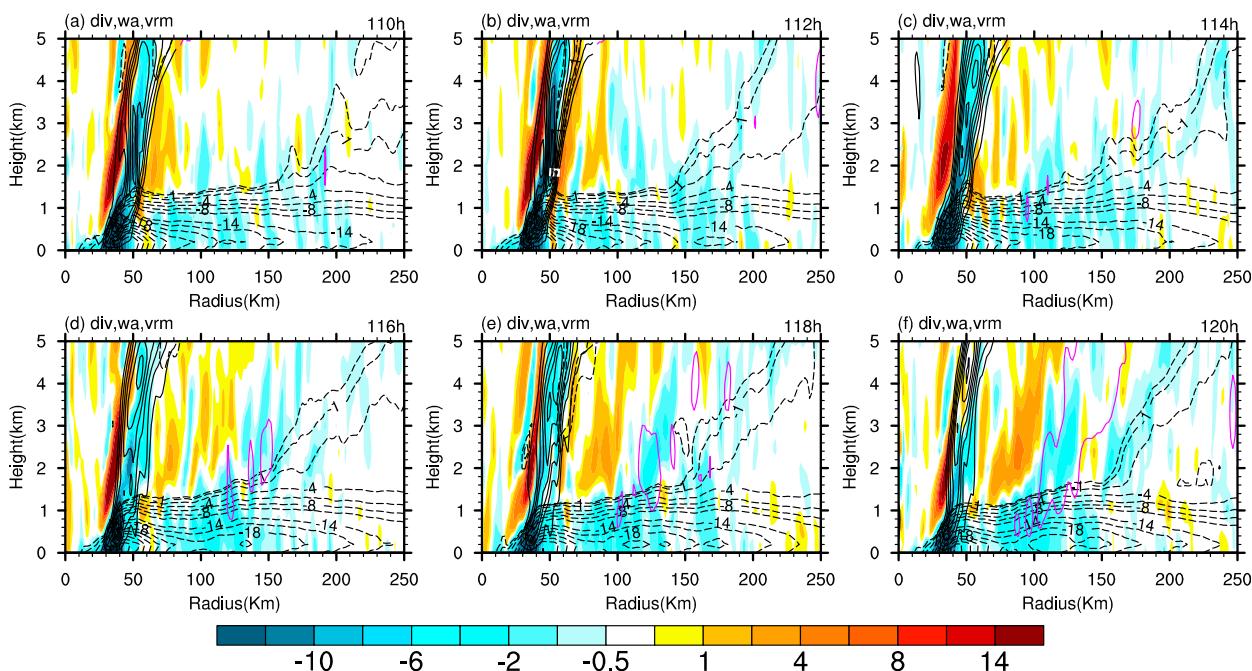


FIG. 4. Radius–height cross sections of the azimuthally averaged divergence (shaded;  $10^{-5} \text{ s}^{-1}$ ), and radial wind (dashed contours;  $\text{m s}^{-1}$ ); contour intervals for radial inflow are  $2 \text{ m s}^{-1}$ . Additionally,  $\pm 0.5$  and  $\pm 1 \text{ m s}^{-1}$  contours are shown to indicate the weak radial flow region and the vertical velocity (black contours are plotted at every  $1 \text{ m s}^{-1}$  in the primary eyewall region; solid magenta contours are plotted at every  $0.5 \text{ m s}^{-1}$  outside the primary eyewall region) from 110 to 126 h at 2-h intervals.

shown below) associated with the large deceleration of the strong boundary layer inflow near the inner edge of the SEF region, a process very similar to that in a single eyewall storm, as demonstrated by Smith and Vogl (2008) and Smith et al. (2009). This dynamical mechanism was applied by Huang et al. (2012) to illustrate the gradual strengthening of the radial inflow and the follow-up inflow convergence in the SEF region.

To measure the degree to which the winds deviate from the gradient wind balance, the agradient force (AF) averaged over and outside the SEF region is examined (Figs. 5c,d). As in many previous studies, the AF is defined as the residual term of the gradient wind balance, which is obtained as the sum of the azimuthally averaged radial pressure gradient force, the Coriolis and centrifugal forces in the radial momentum equation (Huang et al. 2012; Abarca and Montgomery 2013; Qiu and Tan 2013; Sun et al. 2013). A positive (negative) AF implies that the air parcels accelerate outward (inward) where the flow is supergradient (subgradient). The SEF region (Fig. 5c) exhibits a state of relatively weak positive AF ( $12 \text{ m s}^{-1} \text{ h}^{-1}$ ) above the boundary layer from 100 to 110 h. The positive AF above the boundary layer intensifies significantly with time and reaches the magnitude of  $36 \text{ m s}^{-1} \text{ h}^{-1}$  at 120 h, indicating that the wind there is supergradient and accelerating outward. A question arises as to how the boundary layer inflow can

persist in the presence of an outward-directed AF. The strongest enhancement of the boundary layer inflow is in the outer region (Fig. 5b), with almost no enhancement of radial inflow in the SEF region. The AF above the boundary layer in the SEF region is directed outward, and the inflow originating from the outer region tends to decelerate, with a portion of inflow turning upward and outward of the boundary layer. The rest of the boundary layer inflow is still directed inward to the primary eyewall region but does not accelerate with time.

Meanwhile, negative (positive) AF (Fig. 5d) within (above) the boundary layer also intensifies with time in the outer region (between 116- and 150-km radii), but at a much smaller rate (Fig. 5d) than in the SEF region, which is consistent with the fact that the inflow (outflow) below (above) the top of the boundary layer is strengthened only slightly (Fig. 5b). Similar evolutions of the radial wind and the AF in Fig. 5 strongly suggest that the strengthening of inflow, convergence in the boundary layer, and outflow immediately above are primarily attributed to the extent to which the unbalanced process in the boundary layer is suddenly enhanced since the boundary layer is always unbalanced.

In our simulated storm, the timing of the preformation stage (110–119 h) depends largely on when the unbalanced flow in the boundary layer is enhanced. Once the boundary layer inflow is substantially strengthened

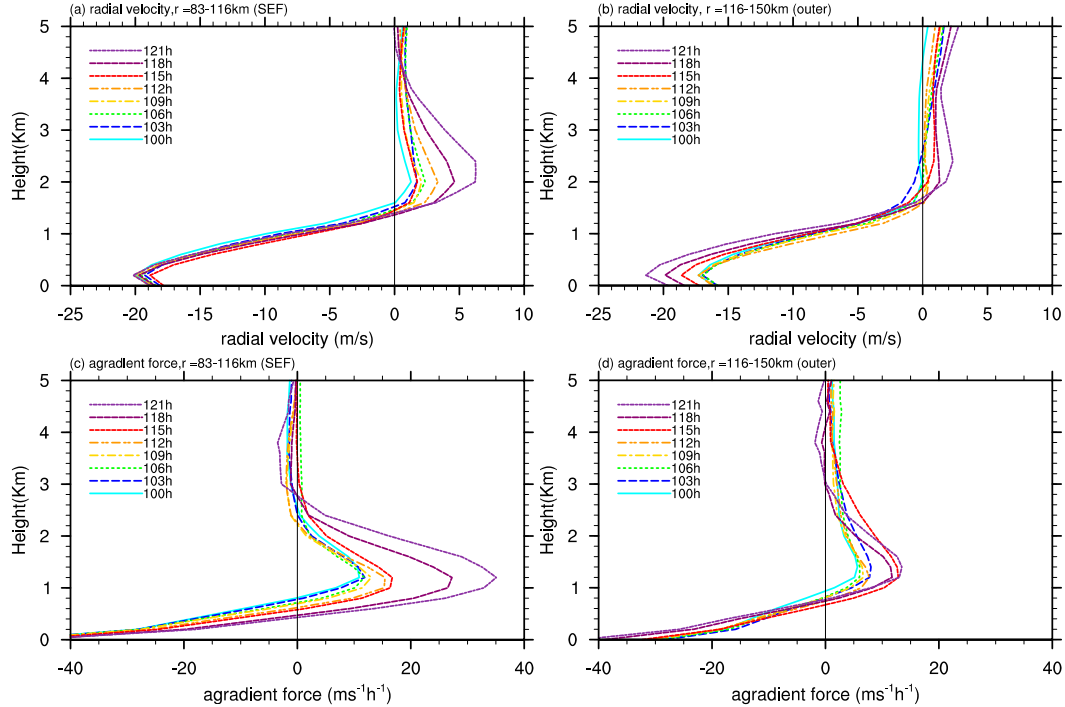


FIG. 5. Area-averaged (a),(b) radial velocity ( $\text{m s}^{-1}$ ) and (c),(d) gradient force per unit mass ( $\text{m s}^{-1} \text{h}^{-1}$ ) over (a),(c) the secondary eyewall (83–116 km) and (b),(d) the outer region (116–150 km) from 100 to 121 h at 3-h intervals.

and decelerated, the boundary layer convergence is established for the upward transport of moist air, which further triggers/enhances convection in the preexisting outer rainbands in the SEF region. Diabatic heating released in the rainbands can also enhance the boundary layer inflow and the moist convergence, enhancing convection in the rainband again and forming a positive feedback mechanism that will be discussed in section 5. Later on, with the emergence of deep convective activity and the resultant acceleration of tangential wind due to the convergence of angular momentum in the SEF region, the rainband becomes more and more axisymmetric, and eventually the secondary eyewall forms as a result of this positive feedback.

To gain insights into the relevant processes that are responsible for the broadening of tangential winds discussed above, we conduct a budget for the azimuthal-mean tangential wind tendency. The budget equation can be presented as

$$\frac{\partial \bar{v}}{\partial t} = -\bar{u} \bar{\zeta}_{\text{abs}} - \bar{w} \frac{\partial \bar{v}}{\partial z} - \overline{u' \zeta'_{\text{abs}}} - \overline{w' \frac{\partial v'}{\partial z}} + \overline{F_{\text{fric}}}, \quad (1)$$

where  $u$ ,  $v$ , and  $w$  are the radial, tangential, and vertical components of the wind, respectively;  $\zeta_{\text{abs}}$  is the vertical component of the absolute vorticity; and  $F_{\text{fric}}$  is the

tangential component of friction and vertical mixing, which is directly derived from the WRF Model simulation. The small term due to horizontal diffusion is omitted here since it is generally one to two orders smaller than the leading terms in (1). The overbar indicates the azimuthal mean, while the prime denotes deviation from the azimuthal mean. The term on the left-hand side of (1) is the azimuthal-mean tangential wind tendency. The five terms on the right-hand side (rhs) are the azimuthal-mean tangential wind tendencies contributed by the radial flux of the azimuthal-mean absolute vorticity by the azimuthal-mean radial wind (mean radial advection), vertical advection of azimuthal-mean tangential wind by the azimuthal-mean vertical motion (mean vertical advection), eddy radial advection, eddy vertical advection, and friction, respectively (Fudeyasu and Wang 2011; Abarca and Montgomery 2014).

Figures 6a and 6b show the radial-vertical cross sections of the actual change of the azimuthal-mean tangential wind and the corresponding change from the azimuthal-mean tangential wind budget as the sum of all terms on the rhs in (1) (diagnosed tangential wind tendency) during the preformation period from 110 to 119 h of simulation using the model output at 6-min intervals. This period is critical to the SEF, as we mentioned above

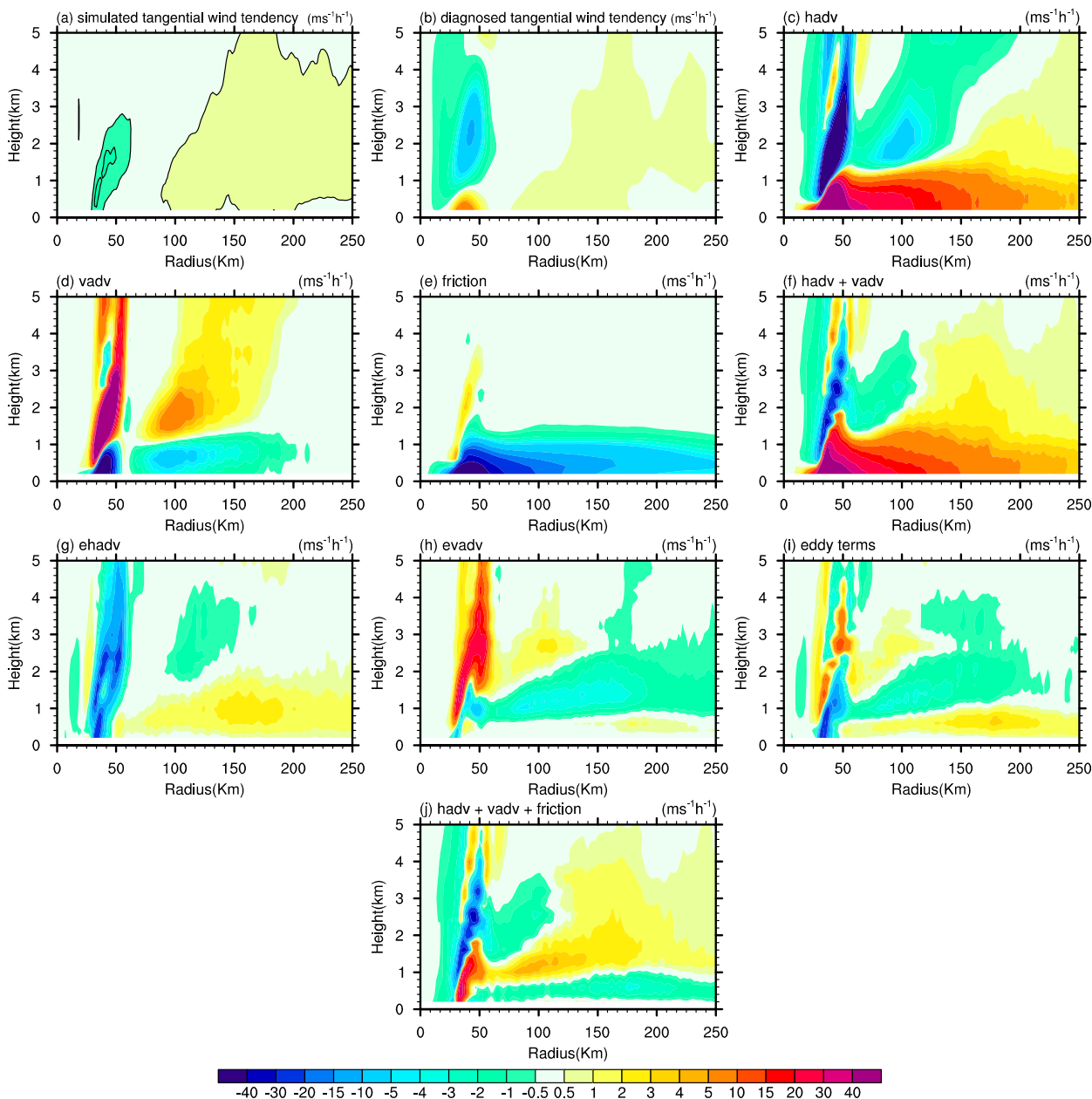


FIG. 6. Radius–height cross sections of the (a) simulated tangential tendency averaged from 110 to 119 h; (b) diagnosed tangential tendency (the sum of all the terms in the tangential wind tendency equation); and tendency of azimuthal-mean tangential wind that is contributed by the following: (c) mean radial advection, (d) mean vertical advection, (e) mean friction term, (f) the sum of the mean radial and vertical advection terms, (g) eddy radial advection term, (h) eddy vertical advection, (i) the sum of the mean eddy radial and vertical advection terms, and (j) the sum of the mean advection terms and the friction term. Tangential wind tendency is presented in  $\text{m s}^{-1} \text{h}^{-1}$ .

(Fig. 3). By the end of this period, features of the secondary eyewall become clear, and the typical concentric eyewall structure appears. From Figs. 6a and 6b, we find that although large differences exist in the inner-core region within a radius of 60 km, the simulated and diagnosed tangential wind tendencies in the azimuthal-mean tangential wind are qualitatively consistent in

most of the SEF region outside the 60-km radius. Therefore, the tangential wind budget can be used to examine processes that are responsible for the broadening of tangential wind and the formation of the secondary tangential wind maximum in the simulation.

The mean radial advection term (Fig. 6c) contributes to the spinup of tangential wind in the boundary layer,

while the vertical advection term (Fig. 6d) shows a negative contribution. The sum of the two mean advection terms (Fig. 6f) is positive in the boundary layer, indicating that the mean radial advection dominates the vertical advection in broadening the boundary layer tangential wind in the simulation. Surface friction (Fig. 6e) is the major term causing the spindown of tangential wind in the boundary layer (Fig. 6h). The mean advection term is balanced to first order by friction, consistent with the findings by Kepert (2013). Above the boundary layer, large positive contributions of the mean vertical advection term (Fig. 6d) are evident in both the primary eyewall and SEF regions where updrafts and diabatic heating occur. These positive contributions are overwhelmed by the negative contribution by the horizontal advection (Fig. 6c), mainly a result of the outflow associated with the supergradient wind, as shown in Fig. 5. However, immediately outside the SEF region, the mean radial advection provides a moderate positive tendency that is distinct throughout the mid- to lower troposphere (Fig. 6c). The combined effect of these two mean advection terms acts to spin up the tangential wind both in the SEF region and immediately outside in the mid- to lower troposphere above the boundary layer (Fig. 6f). In the SEF and the outer regions, the eddy radial advection term (Fig. 6g) is positive not only within but also around the top of the boundary layer (from about the 0.2- to 1.8-km heights). The eddy radial advection term is negative above the 1.8-km height within the SEF region. The positive eddy vertical advection term is quite small and is only present below the 0.8-km height in the SEF and the outer regions. Another positive region is present above the 2-km height within the SEF region. Negative eddy vertical advection terms are located within the SEF region and between the two positive regions. The combined effect of eddy terms (Fig. 6i) contributes negatively to the spinup of tangential wind in the boundary layer of the primary eyewall but contributes positively above the boundary layer. Outside the primary eyewall, the sum of the radial and vertical advection terms due to eddies contributes to spin up tangential wind in the boundary layer, while it contributes to spin down the tangential wind above the boundary layer.

Comparing Figs. 6i and 6j with Fig. 6b, we find that the broadening of tangential wind above the boundary layer prior to the development of radial moisture convergence in the boundary layer and the SEF results mainly from the azimuthal-mean advection of tangential wind. Namely, the inflow in the mid- to lower troposphere in response to both the convective and stratiform precipitation in outer spiral rainbands transports angular momentum inward to spin up tangential winds from the

region outside the SEF region. In response to the broadening of the tangential wind in the mid- to lower troposphere is the development of supergradient flow and radial convergence in the boundary layer. This leads to outflow immediately above the boundary layer and forced upward motion, thus causing strong convection in the SEF region. In the boundary layer, the enhanced radial inflow and convergence spin up tangential wind after the establishment of strong convection in the outer rainbands. However, this spinup is largely offset by surface friction, as shown in Fig. 6j, where the sum of the azimuthal-mean advection and friction contribute negatively to the spinup of tangential wind in the SEF region and farther outward in the boundary layer. This suggests a process for the spinup of the secondary eyewall different from the aforementioned mechanism by Smith et al. (2009) for the spinup of the primary eyewall during the intensification of a TC. We found, however, that during the SEF period, eddies generally play a positive role in the spinup of tangential wind in the boundary layer in the SEF region. In sharp contrast, eddies are unfavorable for the broadening of tangential wind in the mid- to lower troposphere, implying that the formation of the secondary azimuthal-mean tangential wind maximum in the boundary layer and the SEF are partly a result of the eddy angular momentum transport and the axisymmetrization of eddies.

Figure 7 shows the vertical velocity with both the wavenumber-0 and wavenumber-1 structures removed to better examine the evolution of convective-scale perturbations prior to, during, and after the SEF. At 100 h, the convective-scale perturbations (Fig. 7a) are mostly organized in the azimuthal direction of the primary eyewall, inner spiral rainbands (this region later becomes the moat region when SEF occurs), and the tail of inner spiral rainbands (in the southern portion of the later SEF region), showing strong asymmetric structure of the spiral rainbands. The convective-scale perturbations are concentrated over the SEF region with time, an indication of enhanced convective activity as seen in the radar reflectivity field (Figs. 1, 2a). As the spiral rainbands evolve, intense convective cells are organized in the azimuthal direction with nearly no convective-scale perturbations in the moat region at 120 h (Fig. 7e), indicating the formation of the secondary eyewall. The convective-scale perturbations within the SEF region are enhanced, while those in the primary eyewall region start weakening as the process of ERC begins.

From the plan view of the vorticity perturbation field shown in Fig. 8, the distribution of the vorticity couplets is similar to those shown in Didlake and Houze (2011). The positive and negative vorticity perturbations appear in the primary eyewall and the inner spiral rainband

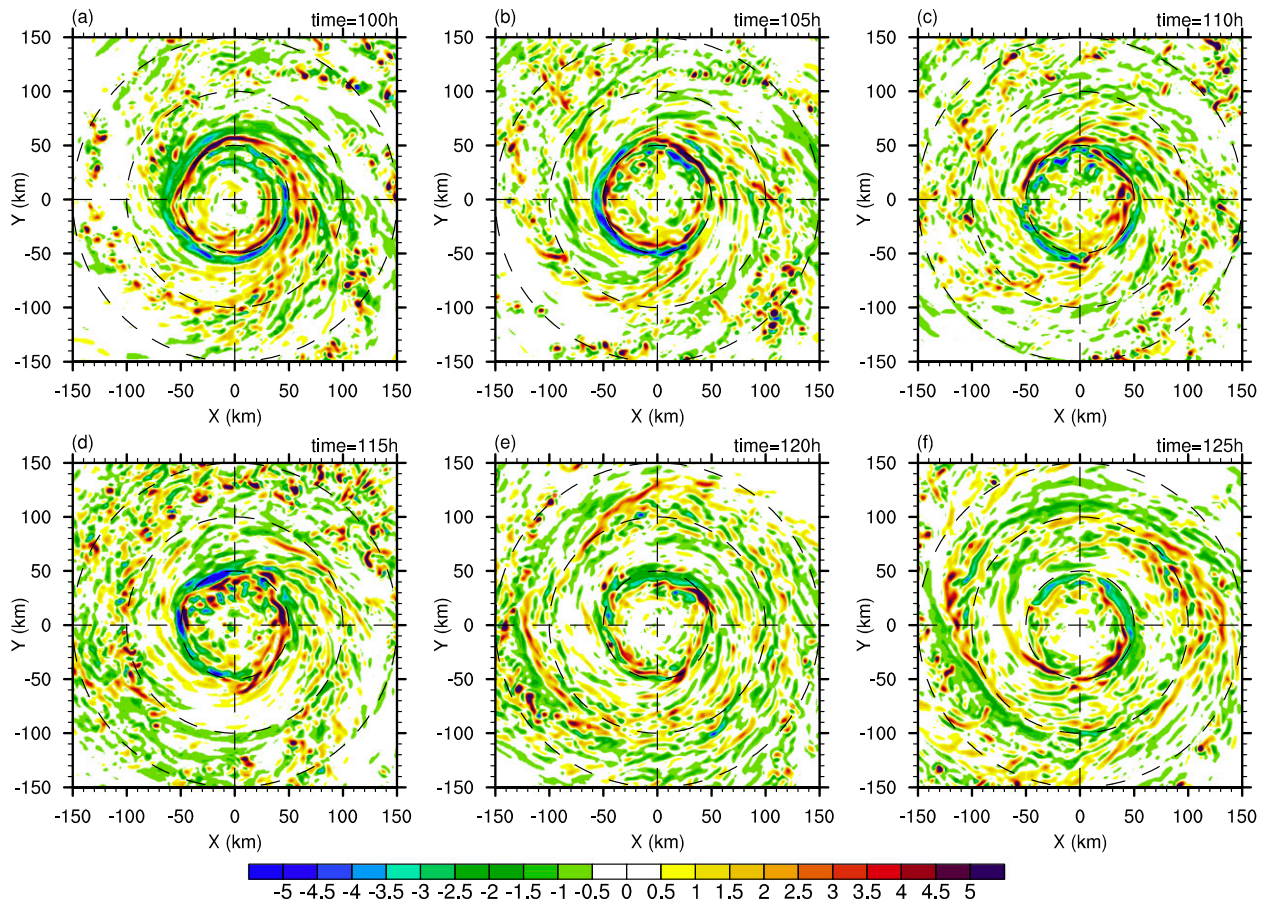


FIG. 7. Plan view of vertical velocity perturbations (shaded;  $\text{m s}^{-1}$ ), which are defined as wavenumber 2 and higher, at 3-km height.

region (future moat region), while limited amounts of vorticity couplets are found in the later SEF region (Figs. 8a–c). The high wavenumber vorticity couplets are gradually concentrated in the SEF region with time after 110 h. This is associated with the development of the convective cells in the outer spiral rainband region (seen in Figs. 1 and 7). At 120 h, very few positive and negative vorticity perturbations are found in the moat region. The lack of vorticity couplets in the moat region is most likely due to the lack of convection. The axisymmetrization of the vorticity perturbation from the outer spiral rainband region is essential for the formation of the secondary eyewall.

To see the asymmetric characteristics of the secondary wind maximum, the vortex is divided into four quadrants. In agreement with the findings of Didlake and Houze (2011), the secondary tangential wind maximum first appears in the quadrants in which the most convective-scale perturbations are embedded (Figs. 9b,c). As the convective cells in the SEF region are being axisymmetrized, both the outer core of the vortex and the tangential wind in the SEF region are strengthened,

and a secondary tangential wind maximum appears, leading to the formation of the secondary eyewall.

## 5. Diagnostics of the balanced contribution

The Sawyer–Eliassen (SE) equation (Eliassen 1951) is a useful tool for investigating the vortex secondary circulation forced by the prescribed heating or momentum forcing or both. The equation has been applied to understand various aspects of TCs (Shapiro and Willoughby 1982; Persing et al. 2002; Montgomery et al. 2006; Bui et al. 2009; Fudeyasu and Wang 2011; Fang and Zhang 2012; Wang 2012; Galarneau et al. 2013), and several studies have also used it to investigate the underlying mechanism that causes the spinup of the secondary circulation related to the SEF (Rozoff et al. 2012; Sun et al. 2013; Abarca and Montgomery 2014; Zhu and Zhu 2014). This section aims to illustrate the extent to which the secondary circulation and the spinup of tangential wind in the SEF region can be explained by the balanced dynamics using the solver of the SE equation introduced in Bui et al. (2009).

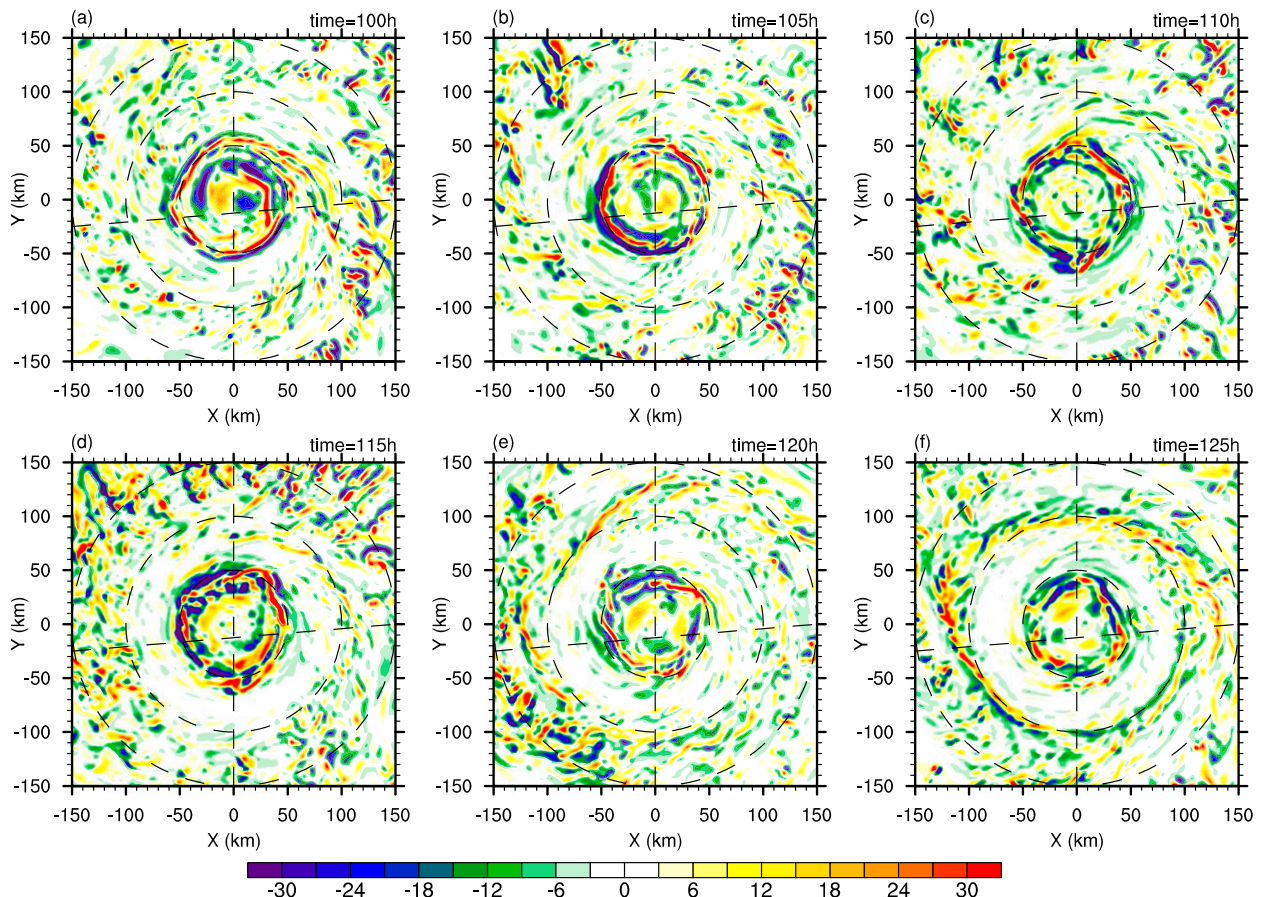


FIG. 8. Plan view of vertical vorticity perturbations (shaded;  $10^{-4} \text{ s}^{-1}$ ) which are defined as wavenumber 2 and higher, at 3-km height.

All quantities used to solve the SE equation are directly derived from the WRF Model simulation at 6-min intervals, converted into the cylindrical coordinates, and azimuthally averaged. The SE equation is solved with a radial grid spacing of 1.67 km (same as in the simulation), while the vertical resolution is uniform with a grid spacing of 0.2 km extending from the surface to the 18-km height. The lateral and top/bottom boundary conditions are the same as those used in Bui et al. (2009) and Fudeyasu and Wang (2011) (with the streamfunction being set to be zero at the axis, bottom, and the top of the computational domain, while the radial gradient of the streamfunction is zero at the lateral boundary). In this study, the radial domain extends to 250 km. We also tried the lateral boundary up to 320 km, but no significant difference in the diagnosed flow field was found (not shown).

Note that there are two regions in which the ellipticity condition of the SE equation is not satisfied in the simulation: one is near the lower boundary, where the vertical shear is quite large, and the other is in the outflow layer, where the inertial stability is negative in some grid

points. To ensure the ellipticity for a numerically converged solution, we simply set the absolute vorticity to be  $10^{-6} \text{ s}^{-1}$  at points where the absolute vorticity is less than zero. If there is any point where the ellipticity is still unsatisfied, the vertical wind shear is reduced, as done in Bui et al. (2009). In addition, our azimuthal-mean tangential wind of the basic TC vortex deviates from the thermal wind balance in the boundary layer. This contributes to the enhanced boundary layer inflow as well (by less than 10%–15% in the surface layer; not shown), in particular in the surface layer, where the inertial stability is much smaller than that implied from the gradient wind.

#### a. Forcing terms from the WRF Model output

Diabatic heating and momentum forcing derived from the simulation averaged over 110–119 h by using the WRF output at 6-min intervals, namely, the preformation period as we identified, are shown in Fig. 10. Strong diabatic heating (Fig. 10a) occurs in the primary eyewall region (at around the 40-km radius) and extends vertically throughout the troposphere with the maximum

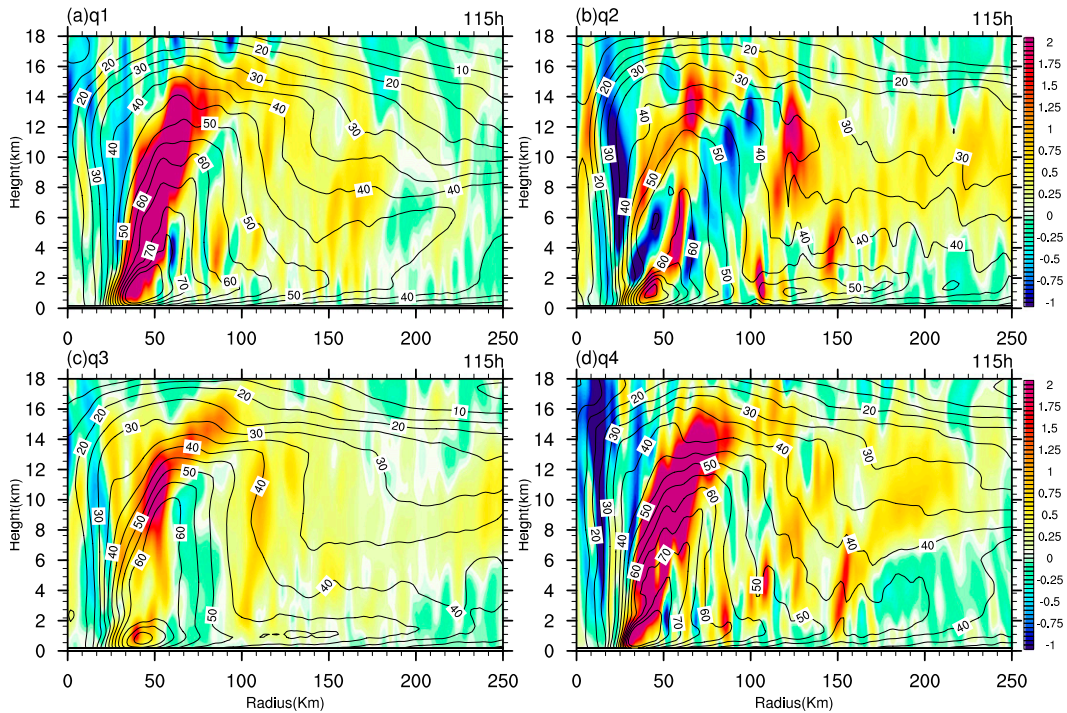


FIG. 9. Tangential wind (contour;  $\text{m s}^{-1}$ , with  $5 \text{ m s}^{-1}$  interval) and vertical velocity (shaded;  $\text{m s}^{-1}$ ) averaged in four quadrants [(a) q1 (northeast), (b) q2 (northwest), (c) q3 (southwest), and (d) q4 (southeast)] at 115 h.

between the 4- and 10-km heights. Cooling can be identified in the mid- to upper troposphere in the moat region. Diabatic heating in the outer-core region, associated with outer rainbands, tilts largely outward and is less pronounced than that in the primary eyewall. The maximum heating rate over this region is about  $20 \text{ K h}^{-1}$  and is located at about the 6-km height. Farther outward, diabatic heating decreases with radius and is maximized in the middle troposphere in the SEF region, while cooling (heating) is shown in the lower (upper) troposphere immediately outside the SEF

region. This heating distribution implies the mixed convective–stratiform nature of precipitation in the outer spiral rainbands (Wang 2009; Li and Wang 2012).

The momentum forcing (Fig. 10b) consists of the azimuthal-mean frictional and vertical turbulent mixing and the azimuthal-mean eddy terms in the azimuthal-mean tangential wind tendency equation [see (1)]. The sink of the tangential wind is largely attributed to the frictional effect and is mainly within the boundary layer, with a maximum value of around  $-50 \text{ m s}^{-1} \text{ h}^{-1}$  in the vicinity of the primary eyewall. Unlike the bimodal

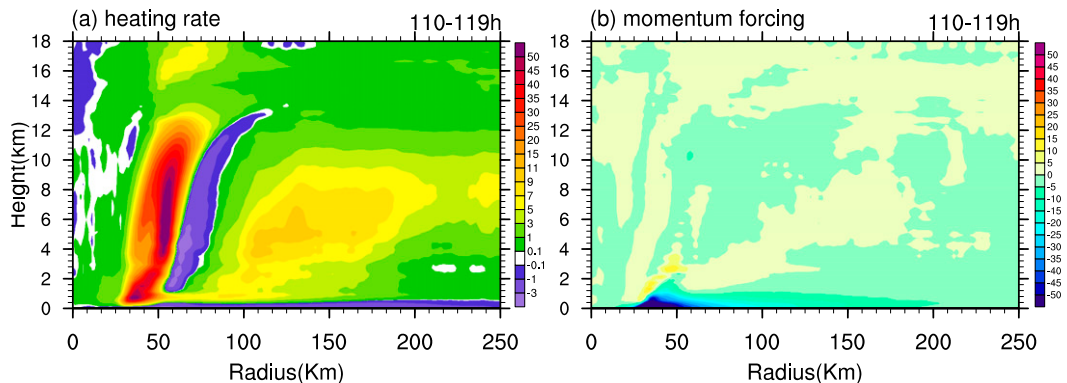


FIG. 10. Radius–height cross sections of the 110–119-h (a) averaged heating ( $\text{K h}^{-1}$ ) and (b) momentum sources ( $\text{m s}^{-1} \text{ h}^{-1}$ ) derived from the WRF Model and prescribed to the Sawyer–Eliassen equation as source terms.

structure in diabatic heating in the radial direction, the momentum forcing over the SEF region does not show any significant increase/decrease in this time period. Note that the positive momentum forcing just above the inflow boundary layer is related to the eddy momentum forcing, as we can see from Fig. 6i.

*b. The secondary circulation diagnosed from the SE equation*

Figure 11 compares the secondary circulation averaged over 110–119 h from the WRF Model simulation with 6-min output and that diagnosed from the SE equation. The mean balanced secondary circulation compares very well with the mean secondary circulation from the WRF simulation both in the pattern and the magnitude, especially in the mid- to lower troposphere. The SE-equation-diagnosed radial inflow in the boundary layer is somewhat weaker inside the RMW and the inner part of the SEF region than that in the WRF simulation (Fig. 12) while being stronger by about  $2 \text{ m s}^{-1}$  in the region outside the SEF region. This difference in the outer region is remarkably close to the

acceleration outside the SEF region shown in Fig. 5b. In the region outside of the 167-km radius, the depth of the inflow layer is underestimated in the SE solution as compared to the WRF simulation. In the SEF region, the discrepancies between the SE-equation-diagnosed inflow and the WRF simulated inflow in the boundary layer are generally small and less than 10%. The outflow immediately above the boundary layer inflow both in the primary eyewall and in the SEF region in the WRF simulation is well captured by the SE equation, which suggests that these features can be reproduced by the balanced dynamics with the prescribed momentum forcing (Fig. 10b). However, the SE solution overestimates not only the inflow in the boundary layer in the outer region, but also the outflow in the middle troposphere (Figs. 11b and 12). Nevertheless, the difference in radial winds between the balanced response and the WRF simulation is relatively small in the SEF region within a radius of 125 km above the boundary layer. Note that the underestimation of boundary layer inflow just inside the RMW and on the inner edge of the SEF region reflects underestimation of the inflow's

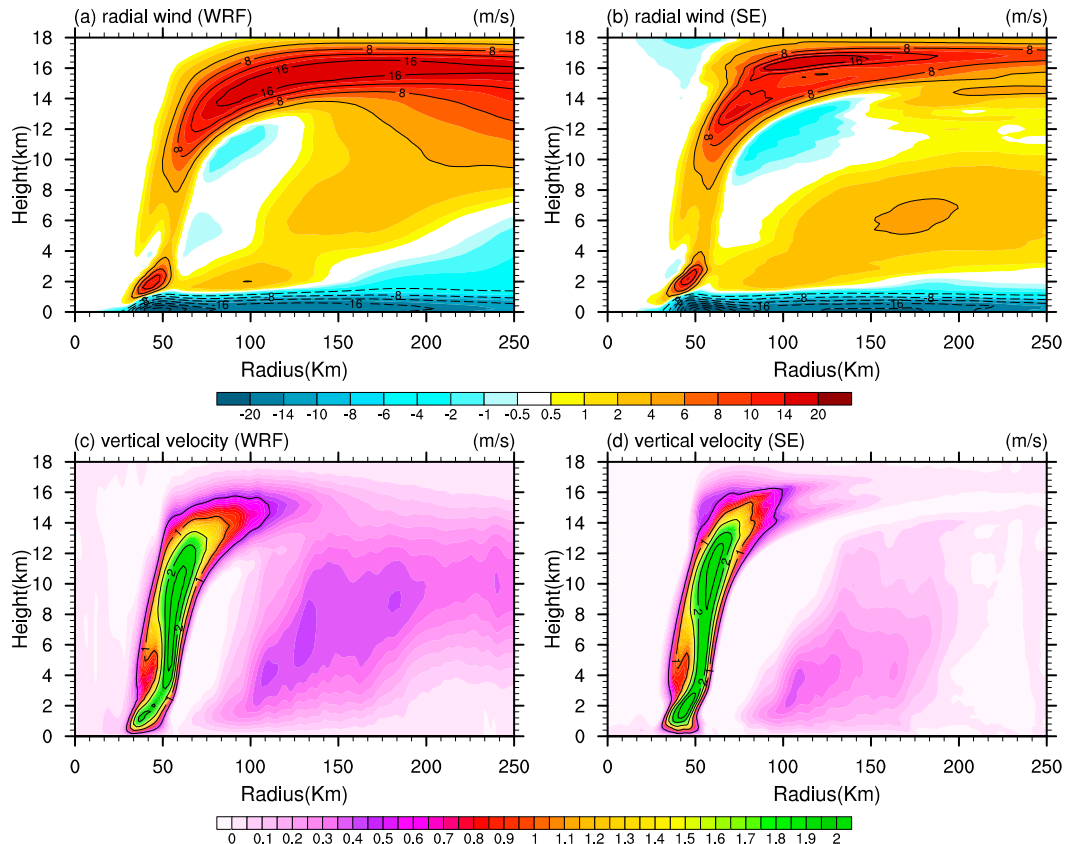


FIG. 11. Radius–height diagrams of (a) WRF-simulated azimuthal-mean radial wind (shaded and contoured according to the color bar;  $\text{m s}^{-1}$ ), (c) vertical velocity (shaded according to the color bar; contoured every  $0.5 \text{ m s}^{-1}$ ). (b),(d) As in (a) and (c), but for the radial wind and vertical velocity diagnosed from the Sawyer–Eliassen equation.

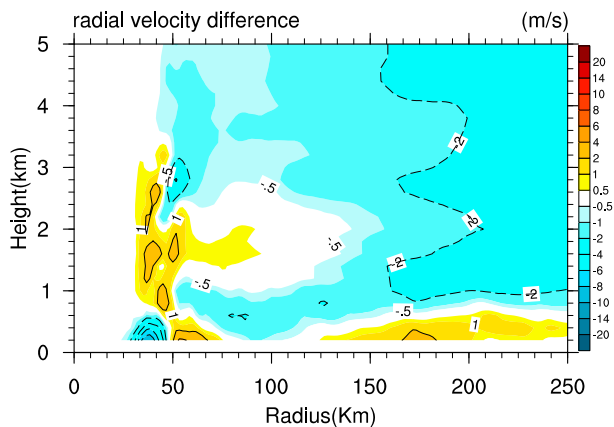


FIG. 12. The difference of the radial velocity between WRF and the Sawyer-Eliassen equation (shaded and contoured;  $\text{m s}^{-1}$ ).

inward penetration across the eyewall and rainbands in the balanced response. This underestimation is similar to the difference between linear and nonlinear boundary layer models, as noted by [Kepert \(2013\)](#).

The pattern of the SE-equation-diagnosed vertical motion ([Fig. 11d](#)) is quite similar to that in the WRF simulation ([Fig. 11c](#)). There are two regions of well-organized vertical upward motion: one is associated with the deep primary eyewall ascent, and the other is primarily originating near the top of the boundary layer in the SEF region and extends outward with height to the radius of about 180 km. The latter is closely related to the activity of spiral rainbands prior to the SEF. The rainband ascent in the SEF region from the SE equation is slightly weaker than that in the WRF simulation, although the balanced boundary layer radial inflow is slightly stronger there compared with the WRF simulation.

From the above comparison, we can conclude that the balanced SE solution can well capture the secondary circulation in the full-physics WRF Model simulation, except for some relatively large discrepancies in the outer region and in the boundary layer. Although the SE-equation-diagnosed boundary layer inflow in the outer region is about  $2 \text{ m s}^{-1}$  stronger than that in the WRF simulation, the boundary layer inflow over the inner core within a radius of 125 km (the SEF region included) is well captured by the balanced dynamics, with differences generally less than 10%. The boundary layer is, to a good approximation, slaved to the parent vortex, as indicated by [Kepert and Nolan \(2014\)](#). The vertical motion from the balanced solution compares well with the WRF simulation, especially in the mid- to lower troposphere. The above results strongly suggest that the balanced framework provides a useful tool for

investigating the response of the secondary circulation to diabatic heating and momentum forcing in the SEF process. We note, however, that our results are inconsistent with the results of [Abarca and Montgomery \(2014\)](#), who found that the balanced dynamics substantially underestimated the secondary circulation in their full-physics model simulation. To clarify the reason why the two studies show such different results, a comparison of the code used to solve the SE equation needs to be done using the same forcing fields, which is beyond the scope of this paper.

### c. Balanced contributions to the tangential wind budget in the SEF region

The balanced contribution to the tangential wind budget in the SEF can be diagnosed by replacing the azimuthal-mean radial wind and vertical velocity in (1) by those diagnosed from the balanced SE equation while keeping other terms directly derived from the WRF simulation. Since the SE equation only solves the azimuthal-mean secondary circulation, we ignore the eddy terms in (2). The tangential wind budget equation then becomes

$$\frac{\partial \bar{v}}{\partial t} = -\bar{u} \bar{\zeta}_{\text{abs}} - \bar{w} \frac{\partial \bar{v}}{\partial z} + \bar{F}_{\text{fric}}. \quad (2)$$

Meanings of the above symbols remain the same as used in (1). [Figure 13a](#) ([Fig. 13b](#)) shows the contribution from the mean radial advection term (the mean vertical advection term) to the tangential wind tendency as calculated by using (2). The mean radial advection term acts to accelerate tangential wind in the boundary layer but decelerate tangential wind in the outflow region immediately above the boundary layer inflow. Similar to the WRF simulation, a relatively strong mean radial advection is observed in the SEF region ([Fig. 13a](#)) in the budget using the balanced flow (cf. [Figs. 6c, 13a](#)). A relatively large difference can be found in the middle troposphere in the outer region, where the stronger outflow in the SE solution leads to a larger negative tangential wind tendency than that in the WRF result ([Fig. 6c](#)). However, the vertical advection of tangential wind ([Fig. 13b](#)) from the balanced calculation is very similar to that from the WRF simulation ([Fig. 6d](#)), both in pattern and in magnitude.

The sum of the two mean advection terms from the SE solution is shown in [Fig. 13c](#). The overall pattern is very similar to the budget from the WRF output ([Fig. 6f](#)) except for some difference in the outer region, where both inflow and outflow are overestimated in the balanced response ([Fig. 12](#)). In the boundary layer, the tangential wind tendency due to the mean advection

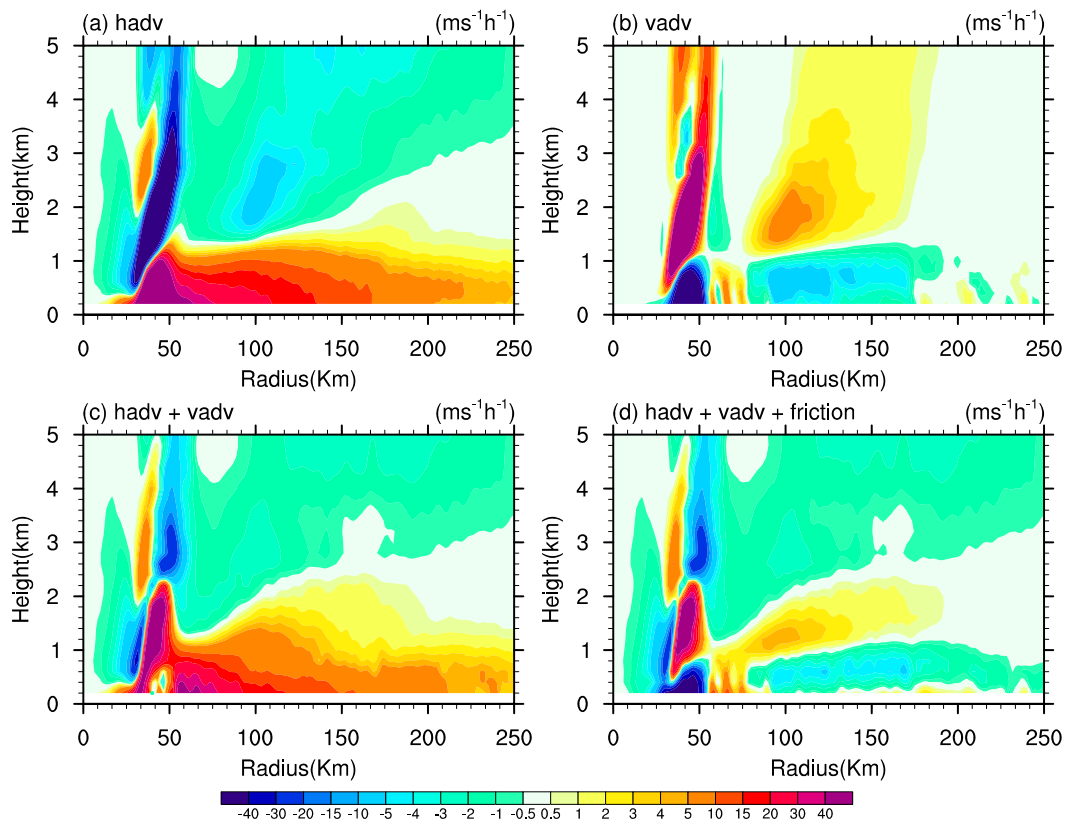


FIG. 13. Radial–height diagrams of (a) mean radial advection term, (b) vertical advection term, (c) the sum of the mean radial and vertical advection terms, and (d) tangential wind tendency from the Sawyer–Eliassen equation. Tendency is shaded according to the color bar ( $\text{m s}^{-1} \text{h}^{-1}$ ).

terms in the SEF region is slightly underestimated (Fig. 13c), consistent with the slightly underestimated boundary layer inflow there (Fig. 12). After the frictional term is included (which is derived from the WRF output as shown in Fig. 6e), the overall pattern of the resultant tangential wind tendency from the SE solution (Fig. 13d) is still similar to that diagnosed from the WRF output (Fig. 6h) except that some differences are visible in the outer-region middle troposphere and in the primary eyewall region. Outside the primary eyewall, the tangential wind tendency is predominantly negative in the boundary layer, and is positive immediately above the boundary layer, consistent with the WRF budget analysis (Fig. 6h). Note that the negative tangential wind tendency in the boundary layer in the SE solution is slightly larger than that in the WRF budget in the SEF region, a result of the underestimated boundary layer inflow in the SE solution. Nevertheless, both the WRF Model simulation and the SE solution show a spindown of tangential winds in the boundary layer by the azimuthal-mean processes. Therefore, the overall spinup in the numerical simulation and in the

tangential wind budget from the WRF Model shown in Figs. 6a and 6b results mainly from the eddy angular momentum transport (Fig. 6i).

Our results demonstrate that the balanced dynamics can capture most of the full-physics WRF Model simulation in terms of the secondary circulation and the tangential wind budget. The result is consistent with the findings of Stern et al. (2015) and Heng and Wang (2016) that the balanced framework could generally reproduce the secondary circulation in response to heating and momentum forcings even though the former used a different linearized equation system. Our result, however, is in sharp contrast to the results of Bui et al. (2009) and Abarca and Montgomery (2014), who showed that the balanced dynamics largely underestimated the secondary circulation and the spin-up of tangential wind in the primary eyewall region or the SEF region. Furthermore, a new finding in our study is the key role played by the eddy processes associated with preexisting spiral rainbands in spinning up tangential wind in the boundary layer, which is thus also critical to the SEF. This eddy–mean flow interaction is accomplished via the

axisymmetrization of eddies, which accelerate the azimuthal-mean tangential wind in the boundary layer.

## 6. Conclusions

To better understand SEF, both balanced and unbalanced contributions to SEF have been discussed in recent years. In this study, the intrinsic internal dynamics responsible for SEF are examined based on an idealized numerical simulation using the three-dimensional full-physics WRF Model.

Our results show that active spiral rainbands with both convective and stratiform natures are maintained and enhanced under favorable thermodynamic conditions with large CAPE over  $1200 \text{ J kg}^{-1}$  between 60- and 250-km radii prior to the SEF. Heating in spiral rainbands is responsible for the tangential wind broadening in the mid- to lower troposphere prior to the SEF and the secondary tangential wind maximum near the top of the boundary layer emerges in the area where the secondary eyewall forms (between 83- and 116-km radii) as a result of the axisymmetrization of eddies in rainbands.

Analysis of the evolution of the radial inflow and the gradient force in response to the broadening of tangential wind above the boundary layer indicates that the strengthening of the boundary layer inflow is primarily attributed to the extent to which the unbalanced process in the boundary layer is enhanced. Once the boundary layer inflow is strengthened, the convergence and the upward motion are enhanced, thus supporting/enhancing convection in the preexisting spiral rainbands. Diabatic heating released in spiral rainbands can in turn enhance the inflow in the boundary layer. This forms a positive feedback process, which can lead to the strengthening of convection in the spiral rainband and eventually the SEF. This process is in agreement with some previous studies (Huang et al. 2012; Abarca and Montgomery 2013, 2014; Wang et al. 2013; Qiu and Tan 2013) that highlighted the importance of the unbalanced process in causing the enhancement of the boundary layer inflow and the spinup of tangential wind in the boundary layer prior to the SEF.

Results from the azimuthal-mean tangential wind budget during the pre-SEF stage demonstrate that the spinup of tangential wind in the SEF region and even farther outward results mainly from the mean radial advection and the eddy angular momentum transport in the boundary layer. The mean radial advection, in turn, is caused by the mid- to lower-tropospheric inflow in response to diabatic heating associated with the preexisting spiral rainbands and not by frictional processes. The eddy angular momentum transport results from eddy-mean flow interaction and the axisymmetrization

of eddies in the spiral rainbands. Our results show that the role of the asymmetric process in spiral rainbands cannot be ignored in this particular idealized simulation of the SEF, although the axisymmetric dynamics becomes dominant after the SEF.

The extent to which the balanced dynamics contribute to the SEF is diagnosed based on the SE equation with heating and momentum forcings from the full-physics WRF Model simulation. The results show that the SE solution can well capture the secondary circulation except for some discrepancies in the diagnosed radial flow in the region outside the SEF both in and above the boundary layer. Overall, the radial inflow diagnosed from the SE equation is within 10% of the full-physics WRF Model simulation in the inner core and the SEF region. The tangential wind tendency associated with the secondary circulation diagnosed from the SE solution is in good agreement with the budget directly derived from the WRF Model output. However, the spinup of tangential winds in the boundary layer in the SEF region could not be explained by the axisymmetric processes (mean advection and friction terms) but is considerably contributed by the eddy angular momentum transport associated with spiral rainbands. This finding indicates that the axisymmetric processes alone could not explain the spinup of tangential wind in the boundary layer, while the asymmetric eddy process appears also to be important to the SEF in this simulation.

In summary, this study demonstrates that the broadening of tangential wind above the boundary layer, an important precursor to SEF as shown in previous studies, is associated with the inward angular momentum transport by the radial inflow in response to diabatic heating in the preexisting spiral rainbands. The unbalanced response to the broadening of tangential wind above is the strengthening of the boundary layer inflow. Although the mean advection associated with the enhanced inflow generally increases the tangential wind, it is offset largely by surface friction outside the RMW. As a result, the axisymmetric processes contribute negatively to the spinup of tangential wind in the boundary layer and thus the formation of the second tangential wind maximum in the SEF region. It is shown that, in addition to diabatic heating, asymmetric eddies in spiral rainbands play an important dynamical role in the spinup of tangential wind in the boundary layer through the eddy-mean flow interaction and axisymmetrization. In addition, it is exhibited that the balanced dynamics can account for over 90% of the secondary circulation in the inner core and in the SEF region, although considerable deviations appear in the outer region. Finally it should be pointed out that, although the idealized simulation can well reproduce the concentric eyewall cycle

similar in many ways (except for the long duration time) to that in observations, the simulated radial location of the SEF could be sensitive to the initial vortex structure and size, the selected model parameterization schemes, and the environmental conditions. Further studies are needed to include those factors and to look into the key processes determining the timing and radial location of the SEF.

*Acknowledgments.* This work is supported by the Ministry of Science and Technology of Taiwan under Grant MOST 103-2628-M-002-004. YW acknowledges financial support from the NSF under Grant AGS-1326524 to the University of Hawai'i at Mānoa and the National Natural Science Foundation of China under Grant 41130964. The authors thank the three anonymous reviewers for their valuable comments.

#### REFERENCES

- Abarca, S. F., and M. T. Montgomery, 2013: Essential dynamics of secondary eyewall formation. *J. Atmos. Sci.*, **70**, 3216–3230, doi:10.1175/JAS-D-12-0318.1.
- , and —, 2014: Departures from axisymmetric balance dynamics during secondary eyewall formation. *J. Atmos. Sci.*, **71**, 3723–3738, doi:10.1175/JAS-D-14-0018.1.
- Bell, M. M., M. T. Montgomery, and W.-C. Lee, 2012: An axisymmetric view of concentric eyewall evolution in Hurricane Rita (2005). *J. Atmos. Sci.*, **69**, 2414–2432, doi:10.1175/JAS-D-11-0167.1.
- Bui, H. H., R. K. Smith, M. T. Montgomery, and J. Peng, 2009: Balanced and unbalanced aspects of tropical cyclone intensification. *Quart. J. Roy. Meteor. Soc.*, **135**, 1715–1731, doi:10.1002/qj.502.
- Didlake, A. C., and R. A. Houze, 2011: Kinematics of the secondary eyewall observed in Hurricane Rita (2005). *J. Atmos. Sci.*, **68**, 1620–1636, doi:10.1175/2011JAS3715.1.
- Dudhia, J., 1989: Numerical study of convection observed during the Winter Monsoon Experiment using a mesoscale two-dimensional model. *J. Atmos. Sci.*, **46**, 3077–3107, doi:10.1175/1520-0469(1989)046<3077:NSOCOD>2.0.CO;2.
- Eliassen, A., 1951: Slow thermally or frictionally controlled meridional circulation in a circular vortex. *Astrophys. Norv.*, **5**, 19–60.
- Fang, J., and F. Zhang, 2012: Effect of beta shear on simulated tropical cyclones. *Mon. Wea. Rev.*, **140**, 3327–3346, doi:10.1175/MWR-D-10-05021.1.
- Fudeyasu, H., and Y. Wang, 2011: Balanced contribution to the intensification of a tropical cyclone simulated in TCM4: Outer-core spinup process. *J. Atmos. Sci.*, **68**, 430–449, doi:10.1175/2010JAS3523.1.
- Galarneau, T. J., Jr., C. A. Davis, and M. A. Shapiro, 2013: Intensification of Hurricane Sandy (2012) through extratropical warm core seclusion. *Mon. Wea. Rev.*, **141**, 4296–4321, doi:10.1175/MWR-D-13-00181.1.
- Gray, W. M., E. Ruprecht, and R. Phelps, 1975: Relative humidity in tropical weather systems. *Mon. Wea. Rev.*, **103**, 685–690, doi:10.1175/1520-0493(1975)103<0685:RHITWS>2.0.CO;2.
- Hawkins, H. F., 1983: Hurricane Allen and island obstacles. *J. Atmos. Sci.*, **40**, 1360–1361, doi:10.1175/1520-0469(1983)040<1360:HAAIO>2.0.CO;2.
- Hawkins, J. D., and M. Helveston, 2008: Tropical cyclone multiple eyewall characteristics. *26th Conf. on Hurricanes and Tropical Meteorology*, Miami, FL, Amer. Meteor. Soc., P1.7. [Available online at [https://ams.confex.com/ams/26HURR/techprogram/paper\\_76084.htm](https://ams.confex.com/ams/26HURR/techprogram/paper_76084.htm).]
- Hence, D. A., and R. A. Houze Jr., 2012: Vertical structure of tropical cyclones with concentric eyewalls as seen by the TRMM Precipitation Radar. *J. Atmos. Sci.*, **69**, 1021–1036, doi:10.1175/JAS-D-11-0119.1.
- Heng, J.-Y., and Y. Wang, 2016: Nonlinear response of a tropical cyclone vortex to prescribed eyewall heating with and without surface friction in TCM4: Implications for tropical cyclone intensification. *J. Atmos. Sci.*, **73**, 1315–1333, doi:10.1175/JAS-D-15-0164.1.
- Hill, K. A., and G. M. Lackmann, 2009: Influence of environmental humidity on tropical cyclone size. *Mon. Wea. Rev.*, **137**, 3294–3315, doi:10.1175/2009MWR2679.1.
- Hong, S.-Y., and J.-O. J. Lim, 2006: The WRF single-moment 6-class microphysics scheme (WSM6). *J. Korean Meteor. Soc.*, **42**, 129–151.
- , Y. Noh, and J. Dudhia, 2006: A new vertical diffusion package with an explicit treatment of entrainment processes. *Mon. Wea. Rev.*, **134**, 2318–2341, doi:10.1175/MWR3199.1.
- Houze, R. A., Jr., and Coauthors, 2006: The Hurricane Rainband and Intensity Change Experiment: Observations and modeling of Hurricanes Katrina, Ophelia, and Rita. *Bull. Amer. Meteor. Soc.*, **87**, 1503–1521, doi:10.1175/BAMS-87-11-1503.
- , S. S. Chen, B. F. Smull, W.-C. Lee, and M. M. Bell, 2007: Hurricane intensity and eyewall replacement. *Science*, **315**, 1235–1239, doi:10.1126/science.1135650.
- Huang, Y.-H., M. T. Montgomery, and C.-C. Wu, 2012: Concentric eyewall formation in Typhoon Sinlaku (2008). Part II: Axisymmetric dynamical processes. *J. Atmos. Sci.*, **69**, 662–674, doi:10.1175/JAS-D-11-0114.1.
- Judt, F., and S. S. Chen, 2010: Convectively generated vorticity in rainbands and formation of the secondary eyewall in Hurricane Rita of 2005. *J. Atmos. Sci.*, **67**, 3581–3599, doi:10.1175/2010JAS3471.1.
- Kain, J. S., and J. M. Fritsch, 1993: Convective parameterization for mesoscale models: The Kain–Fritsch scheme. *The Representation of Cumulus Convection in Numerical Models*, Meteor. Monogr., No. 46, 165–177, doi:10.1007/978-1-935704-13-3\_16.
- Keper, J. D., 2013: How does the boundary layer contribute to eyewall replacement cycles in axisymmetric tropical cyclones? *J. Atmos. Sci.*, **70**, 2808–2830, doi:10.1175/JAS-D-13-046.1.
- , and D. S. Nolan, 2014: Reply to “Comments on ‘How does the boundary layer contribute to eyewall replacement cycles in axisymmetric tropical cyclones?’” *J. Atmos. Sci.*, **71**, 4692–4704, doi:10.1175/JAS-D-14-0014.1.
- Kossin, J. P., and M. Sitkowski, 2009: An objective model for identifying secondary eyewall formation in hurricanes. *Mon. Wea. Rev.*, **137**, 876–892, doi:10.1175/2008MWR2701.1.
- Kuo, H.-C., C.-P. Chang, Y.-T. Yang, and H.-J. Jiang, 2009: Western North Pacific typhoons with concentric eyewalls. *Mon. Wea. Rev.*, **137**, 3758–3770, doi:10.1175/2009MWR2850.1.
- Li, Q.-Q., and Y. Wang, 2012: Formation and quasi-periodic behavior of outer spiral rainbands in a numerically simulated tropical cyclone. *J. Atmos. Sci.*, **69**, 997–1020, doi:10.1175/2011JAS3690.1.

- Martinez, Y., G. Brunet, and M. K. Yau, 2010: On the dynamics of two-dimensional hurricane-like concentric rings vortex formation. *J. Atmos. Sci.*, **67**, 3253–3268, doi:10.1175/2010JAS3500.1.
- , —, —, and X. Wang, 2011: On the dynamics of concentric eyewall genesis: Space–time empirical normal modes diagnosis. *J. Atmos. Sci.*, **68**, 457–476, doi:10.1175/2010JAS3501.1.
- Menelaou, K., M. K. Yau, and Y. Martinez, 2013: Impact of asymmetric dynamical processes on the structure and intensity change of two-dimensional hurricane-like annular vortices. *J. Atmos. Sci.*, **70**, 559–582, doi:10.1175/JAS-D-12-0192.1.
- Mlawer, E. J., S. J. Taubman, P. D. Brown, M. J. Iacono, and S. A. Clough, 1997: Radiative transfer for inhomogeneous atmosphere: RRTM, a validated correlated- $k$  model for the longwave. *J. Geophys. Res.*, **102**, 16 663–16 682, doi:10.1029/97JD00237.
- Montgomery, M. T., and R. J. Kallenbach, 1997: A theory for vortex Rossby-waves and its application to spiral bands and intensity changes in hurricanes. *Quart. J. Roy. Meteor. Soc.*, **123**, 435–465, doi:10.1002/qj.49712353810.
- , M. E. Nicholls, T. A. Cram, and A. B. Saunders, 2006: A vortical hot tower route to tropical cyclogenesis. *J. Atmos. Sci.*, **63**, 355–386, doi:10.1175/JAS3604.1.
- , S. F. Abarca, R. K. Smith, C.-C. Wu, and Y.-H. Huang, 2014: Comments on “How does the boundary layer contribute to eyewall replacement cycles in axisymmetric tropical cyclones?” *J. Atmos. Sci.*, **71**, 4682–4691, doi:10.1175/JAS-D-13-0286.1.
- Moon, Y., and D. S. Nolan, 2010: The dynamic response of the hurricane wind field to spiral rainband heating. *J. Atmos. Sci.*, **67**, 1779–1805, doi:10.1175/2010JAS3171.1.
- Nong, S., and K. Emanuel, 2003: A numerical study of the genesis of concentric eyewalls in hurricanes. *Quart. J. Roy. Meteor. Soc.*, **129**, 3323–3338, doi:10.1256/qj.01.132.
- Persing, J., M. T. Montgomery, and R. E. Tuleya, 2002: Environmental interactions in the GFDL hurricane model for Hurricane Opal. *Mon. Wea. Rev.*, **130**, 298–317, doi:10.1175/1520-0493(2002)130<0298:EIITGH>2.0.CO;2.
- Qiu, X., and Z.-M. Tan, 2013: The roles of asymmetric inflow forcing induced by outer rainbands in tropical cyclone secondary eyewall formation. *J. Atmos. Sci.*, **70**, 953–974, doi:10.1175/JAS-D-12-084.1.
- , —, and Q. Xiao, 2010: The roles of vortex Rossby waves in hurricane secondary eyewall formation. *Mon. Wea. Rev.*, **138**, 2092–2109, doi:10.1175/2010MWR3161.1.
- Rogers, R., S. Lorsolo, P. Reasor, J. Gamache, and F. Marks, 2012: Multiscale analysis of tropical cyclone kinematic structure from airborne Doppler radar composites. *Mon. Wea. Rev.*, **140**, 77–99, doi:10.1175/MWR-D-10-05075.1.
- Rozoff, C. M., W. H. Schubert, and J. P. Kossin, 2008: Some dynamical aspects of tropical cyclone concentric eyewalls. *Quart. J. Roy. Meteor. Soc.*, **134**, 583–593, doi:10.1002/qj.237.
- , D. S. Nolan, J. P. Kossin, F. Zhang, and J. Fang, 2012: The roles of an expanding wind field and inertial stability in tropical cyclone secondary eyewall formation. *J. Atmos. Sci.*, **69**, 2621–2643, doi:10.1175/JAS-D-11-0326.1.
- Shapiro, L. J., and H. E. Willoughby, 1982: The response of balanced hurricanes to local sources of heat and momentum. *J. Atmos. Sci.*, **39**, 378–394, doi:10.1175/1520-0469(1982)039<0378:TROBHT>2.0.CO;2.
- Smith, R. K., and S. Vogl, 2008: A simple model of the hurricane boundary layer revisited. *Quart. J. Roy. Meteor. Soc.*, **134**, 337–351, doi:10.1002/qj.216.
- , M. T. Montgomery, and N. V. Sang, 2009: Tropical cyclone spin-up revisited. *Quart. J. Roy. Meteor. Soc.*, **135**, 1321–1335, doi:10.1002/qj.428.
- Stern, D. P., J. L. Vigh, D. S. Nolan, and F. Zhang, 2015: Revisiting the relationship between eyewall contraction and intensification. *J. Atmos. Sci.*, **72**, 1283–1306, doi:10.1175/JAS-D-14-0261.1.
- Sun, Y. Q., Y. Jiang, B. Tan, and F. Zhang, 2013: The governing dynamics of the secondary eyewall formation of Typhoon Sinlaku (2008). *J. Atmos. Sci.*, **70**, 3818–3837, doi:10.1175/JAS-D-13-044.1.
- Terwey, W. D., and M. T. Montgomery, 2008: Secondary eyewall formation in two idealized, full-physics modeled hurricanes. *J. Geophys. Res.*, **113**, D12112, doi:10.1029/2007JD008897.
- Wang, B., and X. Li, 1992: The beta drift of three-dimensional vortices: A numerical study. *Mon. Wea. Rev.*, **120**, 579–593, doi:10.1175/1520-0493(1992)120<0579:TBDOTD>2.0.CO;2.
- Wang, X., Y. Ma, and N. E. Davidson, 2013: Secondary eyewall formation and eyewall replacement cycles in a simulated hurricane: Effect of the net radial force in the hurricane boundary layer. *J. Atmos. Sci.*, **70**, 1317–1341, doi:10.1175/JAS-D-12-017.1.
- Wang, Y., 2009: How do outer spiral rainbands affect tropical cyclone structure and intensity? *J. Atmos. Sci.*, **66**, 1250–1273, doi:10.1175/2008JAS2737.1.
- , and H. Wang, 2013: The inner-core size increase of Typhoon Megi (2010) during its rapid intensification phase. *Trop. Cyclone Res. Rev.*, **2**, 65–80.
- Wang, Z., 2012: Thermodynamic aspects of tropical cyclone formation. *J. Atmos. Sci.*, **69**, 2433–2451, doi:10.1175/JAS-D-11-0298.1.
- Willoughby, H. E., 1979: Forced secondary circulations in hurricanes. *J. Geophys. Res.*, **84**, 3173–3183, doi:10.1029/JC084iC06p03173.
- , J. A. Clos, and M. G. Shoreibah, 1982: Concentric eye walls, secondary wind maxima, and the evolution of the hurricane vortex. *J. Atmos. Sci.*, **39**, 395–411, doi:10.1175/1520-0469(1982)039<0395:CEWSWM>2.0.CO;2.
- Wu, C.-C., Y.-H. Huang, and G.-Y. Lien, 2012: Concentric eyewall formation in Typhoon Sinlaku (2008). Part I: Assimilation of T-PARC data based on the ensemble Kalman filter (EnKF). *Mon. Wea. Rev.*, **140**, 506–527, doi:10.1175/MWR-D-11-00057.1.
- Zhu, Z., and P. Zhu, 2014: The role of outer rainband convection in governing the eyewall replacement cycle in numerical simulations of tropical cyclones. *J. Geophys. Res.*, **119**, 8049–8072, doi:10.1002/2014JD021899.